

Contents lists available at ScienceDirect

Petroleum Science

journal homepage: www.keaipublishing.com/en/journals/petroleum-science



Original Paper

Insights into the pore structure and hydrocarbon accumulation of lacustrine organic-rich shales



Xiao-Jiao Pang ^{a, b}, Gui-Wen Wang ^{a, b, *}, Yong-Jia Zhang ^{a, b}, Da-Li Yue ^{a, b, **}, Hong-Bin Li ^{a, b}, Li-Chun Kuang ^{a, b}, Chao-Liu Li ^c

- a National Key Laboratory of Petroleum Resources and Engineering, China University of Petroleum (Beijing), Beijing, 102249, China
- ^b College of Geosciences, China University of Petroleum (Beijing), Beijing, 102249, China
- ^c PetroChina Research Institute of Petroleum Exploration and Development, Beijing, 100083, China

ARTICLE INFO

Article history: Received 9 July 2024 Received in revised form 17 September 2024 Accepted 4 December 2024 Available online 7 December 2024

Edited by Jie Hao

Keywords:
Shale oil
Pore structure
Nitrogen adsorption
2D NMR
Hydrocarbon accumulation

ABSTRACT

With the development of unconventional hydrocarbon, how to improve the shale oil and gas recovery become urgent. Therefore hydraulic fracturing becomes the key due to the complicated properties of the reservoirs. The pore structure not only plays an essential role in the formation of complex fracture networks after fracturing but also in resource accumulation mechanism analyses. The lacustrine organicrich shale samples were selected to carry out petrophysical experiments. Scanning Electron Microscopy (SEM) and X-ray Diffraction were performed to elucidate the geology characteristics, MICP, 2D NMR, CT, and N₂ adsorption were conducted to classify the pore structure types. The contribution of pore structure to oil accumulation and hydrocarbon enrichment was explained through the N_2 adsorption test on the original and extracted state and 2D NMR. The results show that micropores with diameter less than 20 nm are well-developed. The pore structure was divided into three types. Type I is characterized by high porosity, lower surface area, and good pore throat connectivity, with free oil existing in large pores, especially lamellation fractures. The dominant nano-pores are spongy organic pores and resources hosted in large pores have been expelled during high thermal evolution. The content of nano-pores (micropores) increases and the pore volume decreases in Type II pore structure. In addition, more absorbed oil was enriched. The pore size distribution of type II is similar to that of type I. However, the maturity and hydrocarbon accumulation is quite different. The oil reserved in large pores was not expelled attributed to the relatively low thermal evolution compared with type I. Structural vitrinite was observed through SEM indicating kerogen of type III developed in this kind of reservoir while the type of kerogen in pore structure I is type II. Type III pore structure is characterized by the largest surface area, lowest porosity, and almost isolated pores with rarely free oil. Type I makes the most contribution to hydrocarbon accumulation and immigration, which shows the best prospect. Of all of these experiments, N₂ adsorption exhibits the best in characterizing pores in shales due to its high resolution for the assessment of nano-scale pores. MICP and NMR have a better advantage in characterizing pore space of sandstone reservoirs, even tight sandstone reservoirs, 2D NMR plays an essential role in fluid recognition and saturation calculation. CT scanning provides a 3D visualization of reservoir space and directly shows the relationship between pores and throats and the characteristics of fractures. This study hopes to guide experiment selection in pore structure characterization in different reservoirs. This research provides insight into hydrocarbon accumulation of shales and guidance in the exploration and development of unconventional resources, for example for geothermal and CCUS reservoirs.

© 2024 The Authors. Publishing services by Elsevier B.V. on behalf of KeAi Communications Co. Ltd. This is an open access article under the CC BY license (http://creativecommons.org/licenses/by/4.0/).

* Corresponding author.

E-mail addresses: wanggw@cup.edu.cn (G.-W. Wang), yuedali@cup.edu.cn (D.-L. Yue).

1. Introduction

Pore space and pore structure are responsible for the storage and seepage capacity of fluid in shales, which play an essential role in oil and gas accumulation mechanism analyses, sweet spot prediction, and carbon capture, utilization, and storage (CCUS)

^{**} Corresponding author.

evaluation (Chalmers et al., 2012; Loucks et al., 2012; Liu et al., 2020; Pang et al., 2022). Moreover, pore structures control the occurrence state of the hydrocarbon and determine the fluid distribution (Zhu et al., 2021; Xu et al., 2022). Overall, analysis techniques of pore structure can be divided into two categories: qualitative characterization and quantitive evaluation. Thin section, scanning electron microscopy (SEM), and field emission SEM (FE-SEM) have been widely applied to describe the geometry morphology of pores and throats (Anovitz and Cole, 2015; Lai et al., 2018; He et al., 2022; Pang et al., 2022). Mercury injection capillary pressure (MICP) (Anovitz and Cole, 2015; Lai et al., 2018; Pang et al., 2022), nuclear magnetic resonance (NMR) (Lai et al., 2018; Pang et al., 2022), gas adsorption (Anovitz and Cole, 2015; Lai et al., 2018), computed tomography (CT) (Tiwari et al., 2013; Liu et al., 2020), transmission electron microscopy (TEM) tomography (Chalmers et al., 2012), atomic force microscopy (AFM) (Vishal et al., 2019), and focused ion beam SEM (FIB-SEM) (Yang et al., 2016; Gou et al., 2019) have been successfully used to quantitively detect pore structure parameters such as porosity, permeability, surface area, pore size distribution, saturation, and so on. Each method has its own advantages and disadvantages.

MICP has been applied widely and successfully in conventional and unconventional (tight sandstone) reservoirs (Clarkson et al., 2013). Mesopores and macropores from nano-scale (3 nm-) can be detected through this technique (Chandra and Vishal, 2021). Pore type, porosity, pore size distribution, and shape and size of throats can be determined. In addition, MICP can also be used to investigate petrophysical properties quantitatively. However, samples used to do MICP tests can not be reutilized due to the pollution of mercury (Anovitz and Cole, 2015; Mastalerz et al., 2021). When the samples are selected from shales characterized by strong heterogeneity, anisotropy, and brittleness, higher mercury injection pressure will break the rocks. While lower pressure can not inject the mercury into the small pores, then micropores therefore will not be probed.

As a non-destructive, sensitive, and quick technique, Nuclear Magnetic Resonance (NMR) has been widely used to investigate petrophysical properties and fluid characteristics. NMR is good for detecting all pores both connected and disconnected pores, and helps determine pore types, permeability estimation, wettability prediction, and fluid occurrence state evaluation under different revolving speed centrifugation tests (Lai et al., 2018; Liu et al., 2020). However, due to the difficulty of examination and calculation of the surface relaxation coefficient of rocks of the unconventional reservoirs, the conversion of pore size distribution from T_2 distribution is hardly realized (Lai et al., 2018; Pang et al., 2022). Pore size data will not be directly obtained through NMR test. In addition, centrifugation experiments can not be carried out due to the lamellation development in the shale of the Qingshankou Formation.

3D high-resolution images comprising pores and throats information will be displayed by CT scanning. Nano-CT and micro-CT can detect pores larger than 16 nm and 500 nm respectively (Tiwari et al., 2013; Liu et al., 2020). Transmission electron microscopy (TEM) tomography, atomic force microscopy (AFM), and focused ion beam SEM (FIB-SEM) can also characterize the spatial distribution (3D visualization) of reservoir space (Chandra and Vishal, 2021). It should be noted that the milling process during imaging will damage the samples and require a lot of care and experience to minimize pore alteration. In this studied region, most of the pores are smaller than 20 nm (He et al., 2022). Both the high cost and shortcomings of not probing micropores make it not the prior option for the characterization of pore structure.

Physisorption has several attributes that make it attractive to use to assess porosity and surface area of complex rocks (Clarkson

et al., 2013; Bai et al., 2022). It exhibits low heats of adsorption so there are no violent or disruptive changes to the samples. It can involve multiple layers of adsorbate, thus allowing for pore measurements as pores, at least small ones, can be filled (Anovitz and Cole, 2015; Liu et al., 2023). Soluble organic matter can be obtained through extraction tests and then the occurrence state of oil can be analyzed (Bai et al., 2022). In addition, adsorption is fully reversible, allowing the adsorbate to fully adsorb and desorb revealing potential hysteresis behavior.

In our study, the XRD test is conducted to analyze petrology characteristics. SEM is applied to qualitatively describe the pore types and occurrence state of shale oil. MICP, NMR, N₂ adsorption, and µm-CT are integrated to classify pore structure types and elucidate pore size distribution. N₂ adsorption before and after dichloromethane extraction is applied to illustrate the occurrence state of hydrocarbon. Samples for different experiments come from different Wells. All of them are carried out to analyze the geological features of unconventional reservoirs. The advantage of each technique in evaluating pore structures is summarized. MICP, NMR, CT, and N₂ adsorption were used to divide pore structures, in which, N₂ adsorption was used as the basic one since the reservoir space was dominated by nano-scale and micropores in shales. Four classifications of pore structures using various methods are constructed to ensure the accurate division of the pore structures. N₂ adsorption and 2D NMR under different conditions are favorable for the analyses of hydrocarbon generation and immigration as well as oil occurrence state. The T_1 - T_2 maps and T_2 spectra derived from 2D-NMR tests under different conditions assisted in verifying the hydrocarbon accumulation mechanism.

2. Theory and methods

2.1. X-ray diffraction

Each mineral crystal has a specific X-ray diffraction spectrum, and the characteristic peak intensity in the spectra is positively correlated with the content of the mineral in the sample. The value of the positive correlation between the content of a mineral and the intensity of its markers can be determined experimentally. Then the content of the mineral can be calculated by measuring the characteristic peak intensity in the unknown sample.

XRD analyses were finished using D/max-2200 X-ray diffractometer (No. 2035C4) according to the criteria of SY/T 5163—2018 at the Geological Laboratory Research Institute of E&D Daqing Oil Field Company Ltd. Samples were firstly crushed to powder (<200 mesh). Then, the prepared samples were placed in a rectangular holder and pressed to form a uniform layer and the container was mounted into the instrument. After the tube voltage and current generator were set, the X-ray beam was applied to scan the sample from various angles. Consequently, the data acquisition and associated software were used to define the minerals following the criteria (Rietveld method) (Kamble et al., 2022). Facilities were working at a temperature of 20 °C and humidness of 40%.

2.2. SEM

When the sample was scanned by electron beam, the electron beam in the cathode ray tube would scan synchronously. Then, the signals excited by the electron beam on the sample can be caught by the detector, which was useful for adjusting the electron beam intensity in the image tube. Consequently, the electron micrograph of the sample can be obtained. Mineral composition and pore throat structures can be identified.

The core samples were cut into $5\times5\times3$ mm and polished and sprayed with a layer of gold on the surface for the SEM test. It was

performed on JSM-5600 L V SEM (No. MP17500087) with the standard SY/T 5162–2014 at Geological Laboratory Research Institute of E&D Daqing Oilfield Limited Company Ltd. The test environment was set at 20 $^{\circ}\text{C}$ and 38% humidity. SEM analysis is one straight and repeatable method of illustrating the mineral composition, especially clay mineral types and pore system, especially micro-nano scale pores.

2.3. MICP

MICP test, a good way to estimate the connectivity pores and throats. With the increasing applied pressure, the volume of mercury injected into the pores increases. The smaller the pore size, the higher the pressure required (Eq. (1)) (Chalmers et al., 2012; Chen et al., 2021). 200 MPa is commonly utilized as the highest applied pressure in shale oil and gas reservoirs since the sample will be destroyed by overpressure. The pressure is up to 413 MPa (59,885 psi) in tight sandstone reservoirs, thus, the pore size ranging from 1.78 to 4,750,000 nm can be detected (Lai et al., 2018; Shen et al., 2022). Additionally, pore volume corresponding to various pores and throats can be determined by the quantity of injected mercury.

$$r = -\frac{2\gamma\cos\theta}{P_{\rm c}}\tag{1}$$

where r is the pore throat radius. θ is the contact angle, which is commonly in the range of $135^{\circ}-145^{\circ}$ with an average of 140° between the rocks' surface and the mercury. The surface tension γ is 0.48 N/m and $P_{\rm c}$ is the mercury injection pressure with unit of MPa. Thus Eq. (1) can be simplified to Eq. (2).

$$r = \frac{0.736}{P_{\rm c}} \tag{2}$$

In our study, MICP test was executed at Fluid Mechanics Laboratory at Exploration and Development Research Institute of Daqing Oilfield Co. Ltd using AutoPore IV 9505 Pore Analysis Instrument (No. 34140898). This test was conducted under an environment of 25.5–26.5 °C and humidity in the range of 8%–10%. Then samples selected from the Cretaceous Qingshankou Formation, Gulong Sag in Well GY 1, were cut into plug before. The maximum operating pressure was 200 MPa (29,000 psi), indicating that the smallest pore throat radius detected was approximately 3.7 nm according to the Washburn Equation (Eq. (1)). Pore structure parameters including porosity, permeability, pore and throat radius, threshold pressure, and mercury withdraw efficiency can be obtained. Therefore, pore structure types can be divided according to these parameters and the curves.

2.4. Two-dimensional NMR test

Due to the advantage of being non-destructive and fully pore size (both small and large pores) being tested, NMR is favorable for the determination and analysis of the pore structure of sedimentary rocks. Moreover, two-dimensional NMR (2D NMR) plays a significant role in fluid assessment since both longitude relaxation time (T_1) and transverse relaxation time (T_2) can be obtained, which can separate different fluids present precisely and evaluate fluid behavior (Washburn et al., 2015; Sigal, 2015; Liu et al., 2020). Low field (2 MHz) 2D NMR test was executed at PetroChina Research Institute of Petroleum Exploration and Development. The inversion recovery was adopted in the data acquisition of 2D-NMR test. The echo strings are set as 30, in which the minimum T_1 value is 0.02 ms, the maximum T_2 value is 569.3 ms. The scan number, gain value, wait time, and interval between echoes are 128, 40, 1 s, and

0.1 ms, respectively. 11 samples drilled from Wells SS and WW were prepared into a cylindrical shape and then put into the instrument. Three conditions of samples were set and detected, including as received (AS), after being dried at 105 °C (D), and kerosene imbibed (KI). During the measurement process, The T_2 spectrum will be generated, which was utilized to interpret the pore size distribution. Generally, longer relaxation time represents larger pores. Conversely, the short T_2 component indicates small pores. However, the pore size distribution cannot be directly obtained by T_2 spectra until a conversion of the T_2 is performed (Eq. (3)) (Li et al., 2015; Pang et al., 2022). Therefore, the T_2 spectra can be converted to the pore size distribution diagram.

$$r = \rho_2 F_{\mathsf{S}} T_2 \tag{3}$$

where r is the pore radius, ρ_2 is the surface relaxivity, which is utilized for depicting the rock property and in this study, it is defined as 4.37 nm/ms according to previous studies (Zhao et al., 2020; Li et al., 2020). F_s is the geometric shape factor. F_s values of 2 and 3 represent cylindrical pores and spherical pores, respectively. In this work, F_s was to 2 according to the SEM observation of pores. T_2 is the transverse relaxometry.

2.5. N₂ adsorption

Under a certain temperature and pressure, the surface of molecular sieve particles (adsorbent) has a reversible physical adsorption effect on N_2 . Moreover, there is a definite equilibrium adsorption amount under the corresponding pressure. According to the data of pressure and the N_2 quantity adsorbed, the N_2 adsorption-desorption curve can be obtained. The shape of adsorption isotherm is directly related to pore size and pore number. The isotherm is divided into six types named IUPAC classification by Brunauer, Emmett, Teller, and Sing (Fig. 1) (Sing et al., 1985; Anovitz and Cole, 2015; Thommes et al., 2015; Liu et al., 2020; Wang et al., 2022).

The shapes and size of the hysteresis loops can also be used qualitatively to infer details about the pore structure and the pore types encountered by N₂ during the sorption test. Types IV is further divided into four subtypes: H1, H2, H3, and H4 (Fig. 1) (Sing et al., 1985; Thommes et al., 2015; Liu et al., 2020). Although both BJH and DFT models were used to illustrate pore size distribution, a subtle distinction existed between these two. The pore size distribution curve calculated by DFT model displayed multiple peaks and more detailed information than that by the BJH model. This is because both molecular dynamic and Monte Carlo simulations are utilized alternatively by DFT model (Chen et al., 2021). Thus, heterogeneous reservoirs could be characterized accurately (Chen et al., 2021). While, the BJH model extract pore size distribution from isotherm data using only Kelvin formula, which presumable result in the over large volume of small pores (Li et al., 2015). This also can be found in our study as shown in Fig. 2. Thus, in our later study, all the pore size distributions are generated from DFT model.

The N_2 gas adsorption-desorption analyses were conducted at the Exploration and Development Research Institute of Daqing Oilfield Co. Ltd. The test processing was performed in strict accordance with the Standard of GB/T 21650.3 USING ASAP 2460 3.01. Total 38 samples obtained from Well 8 H C were selected to do nitrogen sorption test. Brunauer-Emmet-Teller (BET), Barrett-Joyner-Halenda (BJH), and DFT models were used to calculate the surface area, pore volume and average pore size, and pore size distribution characteristics of specific surface area and pore volume, respectively.

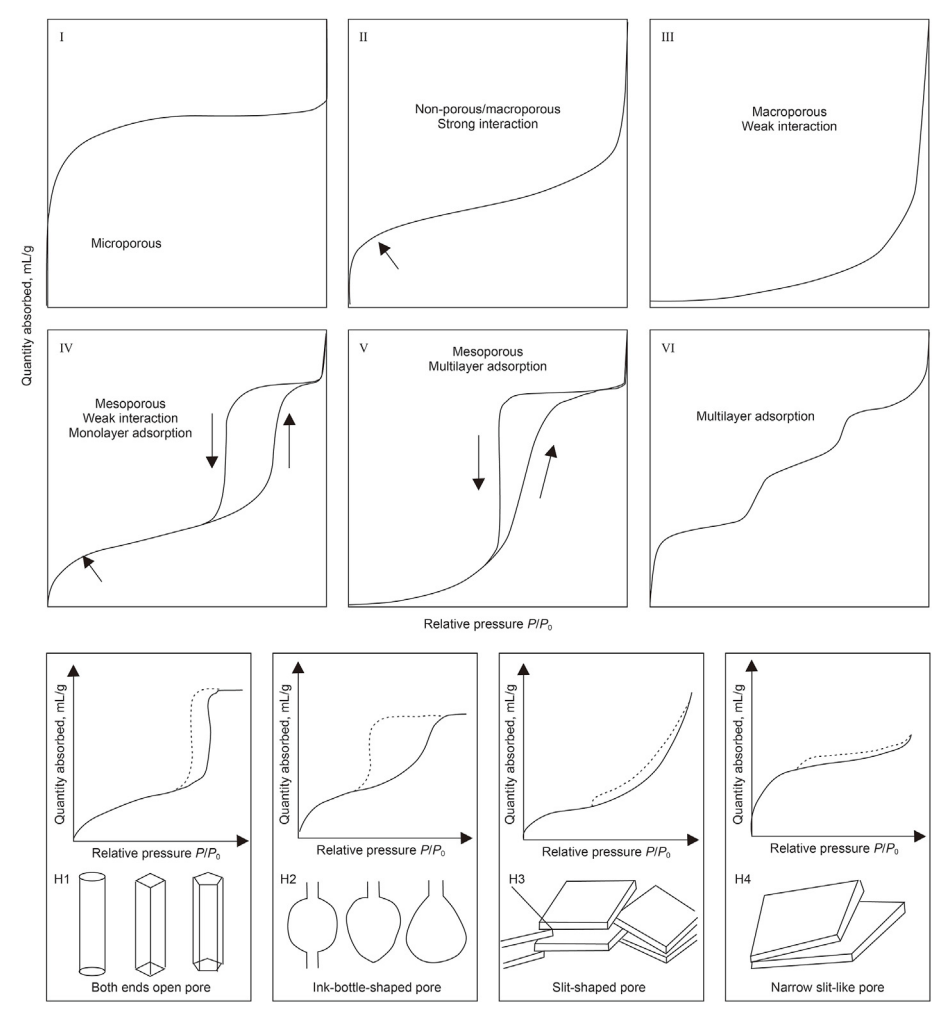


Fig. 1. Types of physisorption isotherms and hysteresis loops and corresponding pore types.

2.6. CT scanning

Three-dimensional X-ray scanning, a non-destructive technique, is used to determine pore structures in 3D space (Ikeda et al., 2000; Chandra and Vishal, 2021; Gou et al., 2021). According to the density and chemical composition differences of minerals and fluids, various components can be identified by grayscale values during computed tomography (CT) scanning (Ikeda et al., 2000; Liu et al., 2023). For example, bright white and dark gray represent pyrite and organic matter, respectively. Light gray indicates quartz and clay minerals. Pores and fractures will be captured as dark (Liu et al., 2023). Then the 3D image of the shale samples will be reconstructed by software. Pore and throat spatial distribution, connectivity of pores and throats as well as fractures will be displayed. Total 21 samples were selected from the Qingshankou Formation in Well GY1 to conduct Micro-CT scanning test.

Fig. 2 shows the characteristics of pore size distribution derived from N_2 adsorption, MICP, and NMR tests. All of them can be used to characterize pore structures. MICP show more information about connectivity of pores and throats, but miss nano-scale and micro small pores. Both isolated and connected pores can be described by NMR test. Usually, oil-bearing property can be obtained through NMR tests under different centrifugation speeds. However, samples collected for this study can not carry on centrifugation tests attributing to the characteristics of multi-scale laminated structure. These samples will be crushed under pressure. While N_2 adsorption

analysis provides more detailed information about micro-pores and mesopores. Combined with extraction N_2 sorption experiment, the hydrocarbon accumulation features of the shale oil reservoir in the Qingshankou Formatoin will be unraveled.

3. Results

3.1. Geology characteristics

3.1.1. Mineral composition

The selected samples show that the primary minerals of the Cretaceous Qingshankou Formation are quartz, feldspar, and clay, followed by calcite, ankerite, and pyrite with an average of 32%, 22.1%, 29.9%, 6.2%, 5.8%, 3.3%, respectively (Fig. 3(a)). The Qing 1 Member is characterized by higher clay content with an average value of 32.8% and lower feldspar (Fig. 3(b)). The content of carbonate in some samples is up to 90%, attributed to the development of shelly creatures (Pang et al., 2023). Therefore, shelly limestone can be observed in some depth, indicating a decrease in the lake level (Pang et al., 2023). Dolomite can also be seen. However, these carbonates only account for 15%, which is less common in the studied succession (Pang et al., 2023). The primary lithology of the Qingshankou Formation is shale, including argillaceous shale, felsic shale, carbonate shale, and mixed shale (Liu et al., 2019). The clay consists of illite, kaolinite, chlorite, illite/smectite mixed layer, and chlorite/smectite mixed layer. Illite is the main clay mineral,

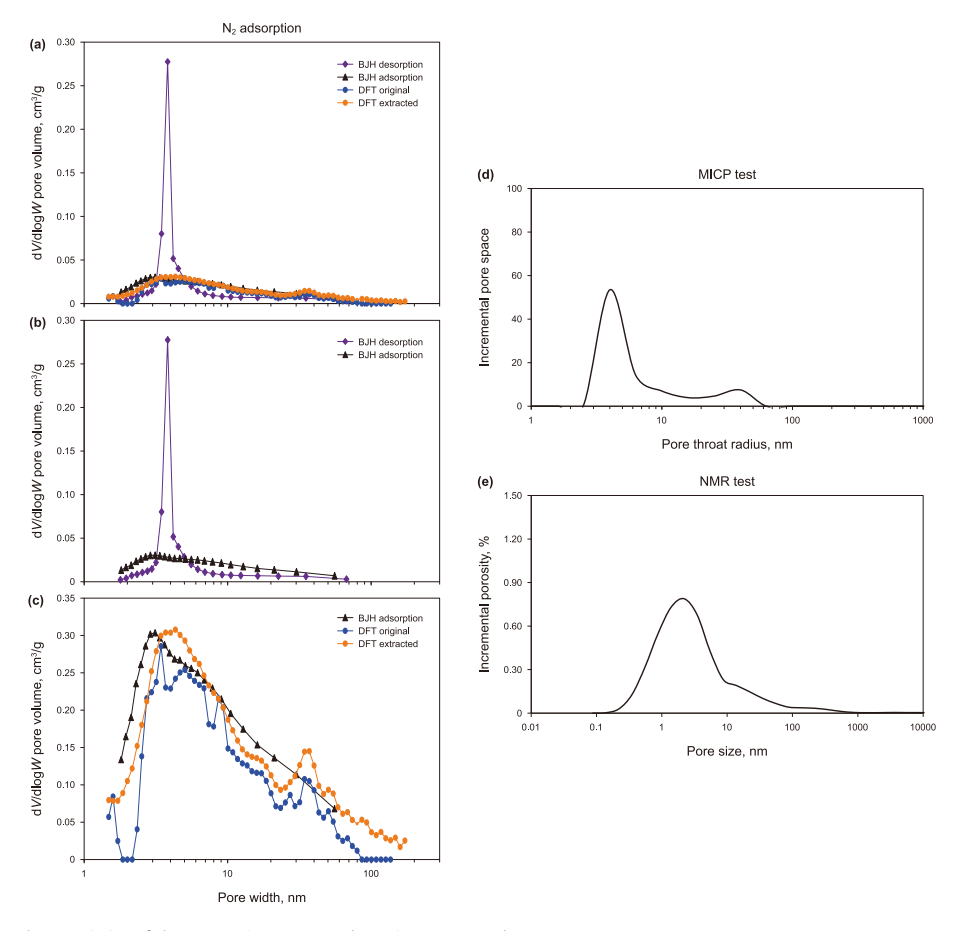


Fig. 2. Pore size distribution characteristics of three experiments: N₂ adsorption, MICP, and NMR. **(a)** N₂ sorption curves derived from BJH and DFT models. **(b)** N₂ sorption curves obtained from BJH models. **(c)** N₂ sorption curves obtained from DFT models show more pore size distribution characterizations. **(d)** Pore size distribution is tested by MICP. **(e)** NMR shows pore and throat distribution.

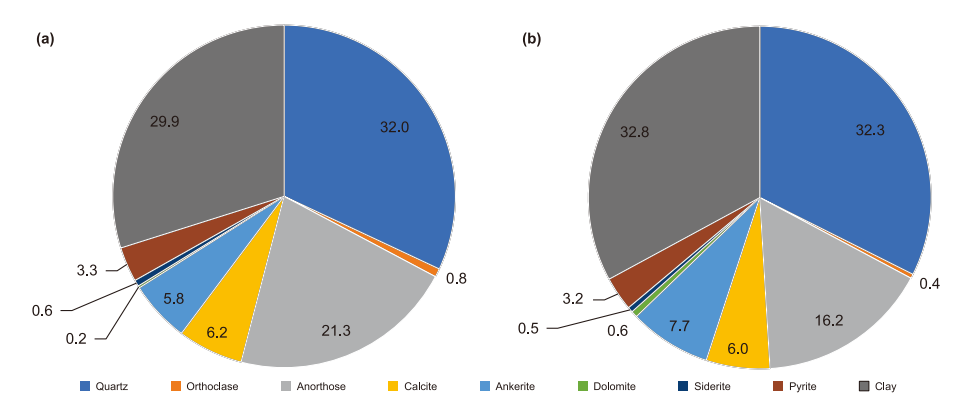


Fig. 3. Mineral composition of the Qingshankou Formation in the Gulong Sag, Songliao Basin. **(a)** The mineral composition of the Qingshankou Formation, total 794 samples. **(b)** The mineral composition of the Qingshankou Formation, total 316 samples.

followed by chlorite and illite/smectite mixed layer. Kaolinite and chlorite/smectite mixed layer are rarely developed.

3.1.2. Pore types

As observed in the SEM images, the pore types are intraparticle dissolution pores, mainly occurring in feldspar (orthoclase and anorthose), rarely observed in quartz, interparticle dissolution pores, lamellation fractures, intercrystallite pores, organic matter pores, and micro-fractures (Fig. 4). Organic matter pores and intragranular pores are the main pores, followed by intergranular

pores. Most of the pores are isolated from each other unless they are connected by lamellation fractures. The shapes of throats are flakes, curved flakes, ink bottles, and tubes. The dissolution and compaction during thermal evolution and diagenesis enlarge the pore size and enhance the lamellation, which improves the reservoir quality (an increase of both permeability, porosity, and pore throat connectivity).

3.1.3. Oil occurrence status

Previous studies have shown that Gulong shale has good

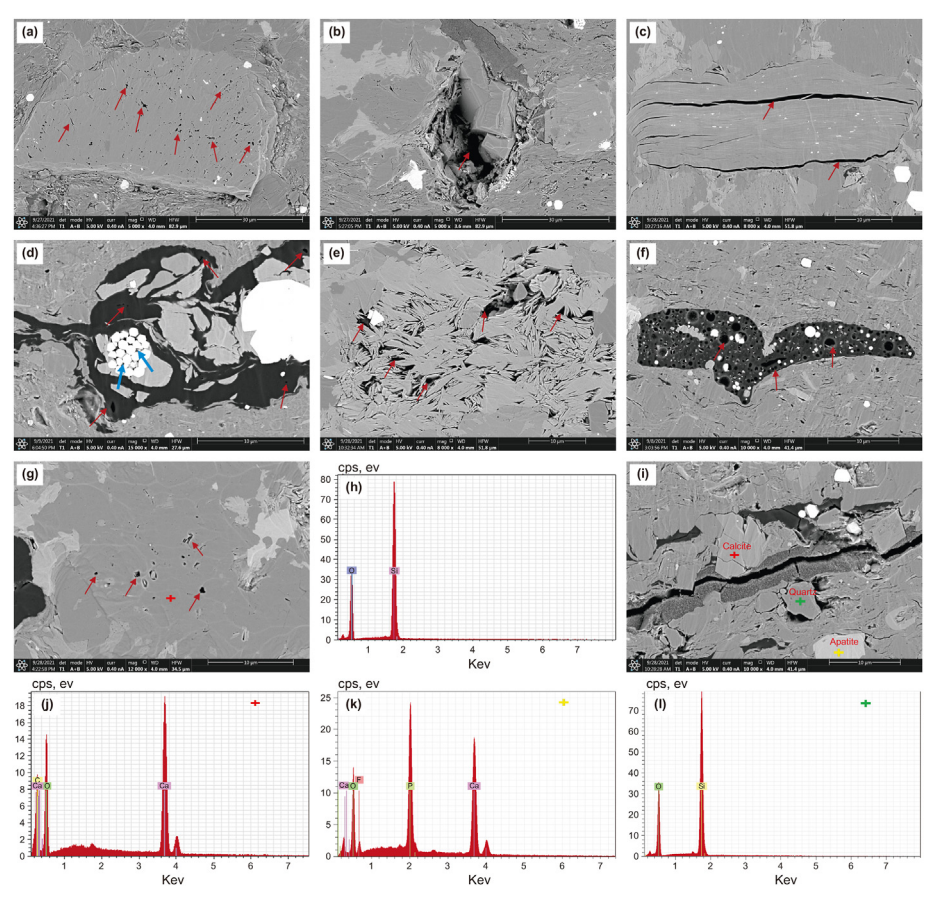


Fig. 4. Pore types observed by SEM. **(a)** Orthoclase intraparticle dissolution pores, 2323.6 m, Well Z. **(b)** Interparticle dissolution pores, 2329.15 m, Well Z. **(c)** Micro fractures, 2337.1 m, Well Z. **(d)** Pyrite intragranular pores (blue arrows) and organic matter pores (red arrows), 2347.1 m, Well Z. **(e)** Chlorite intercrystallite pores, 2337.1 m, Well Z. **(f)** Organic matter pores, 2351.1 m, Well Z. **(g)** Quartz intraparticle dissolution pores, 2353.1 m, Well Z. **(h)** Quartz, EDS of (g). **(i)** Micro fracture, 2337.1 m, Well Z. **(j)** Calcite, EDS of red cross in (i). **(k)** Apatite, EDS of yellow cross in (i).**(l)** Quartz, EDS of green cross in (i).

resource potential, and oil and gas exist in various types of reservoir spaces (Huangfu et al., 2023; He et al., 2023). The free oil mainly occurs in large pores and fractures, especially lamellation fractures, which make the most important contribution to productivity. Adsorbed oil mainly hosts in organic pores, intergranular pores, and intragranular pores. From optical microscope observation, shale oil is abundant in lamellation fractures (Fig. 5(a)-(c)). According to SEM images, shale oil on the surface of organic matter can be seen to gather in the form of oil film, mostly distributed along the edge of pores (Fig. 5(d)-(e)). From the Laser Scanning Confocal Microscope observation, the content of light oil increases with the increase of maturity (Zhang et al., 2021; Liu et al., 2019). Light hydrocarbon components have good fluidity and are more easily distributed and accumulated along the lamellation fractures. The circular organic pores indicate the escape of low-carbon hydrocarbon (Fig. 4(f)). Reservoirs with high organic matter content are more likely to enrich crude oil. When the lamellation fractures are not developed, the crude oil mainly accumulates in the matrix pores (Liu et al., 2018; Zhang et al., 2021).

3.2. Pore size distribution

3.2.1. MICP analysis results

The mercury injection curve and pore size distribution of ten tested shale samples are shown in Fig. 6(a)—(b). The intrusion- and extrusion curves show different features implying complex pore structures and sedimentary environment (Fig. 6(a)). The injection

curve is controlled by pore-throats whereas the extrusion curve is controlled by pore radius and pore connectivity (Anovitz and Cole, 2015). The length of the plateau region of the injection curve represents the connectivity of the pores and throats. The longer the plateau region, the better the connectivity. The pore sizes range from almost 3.7 to 3000 nm, of which the larger part (<20 nm) represents the micro- and meso-pores while a smaller part (>100 nm) indicates microfractures or lamellation fractures (Fig. 6(b)). Due to the limit intrusion pressure, pore systems smaller than 3.7 nm cannot be revealed. The pore size distribution curves are characterized by unimodal and left-skewed implying the pore sizes are dominated by mesopores (Fig. 6(b)). Only a few curves exhibit bimodal behavior representing complicated pore structure, with both small and larger pores coexisting. As evident from Table 1, R_p is in the range of 8–494 nm, with an average value of 81 nm, but mostly concentrates around 10 nm. The data of the pore size distribution peak illustrate that the pore size is mainly distributed around 6 nm (Table 1). According to the permeability distribution analysis, at the size of $R_{\rm f}$, the permeability contribution viz $F_{\rm m}$ ranges from 43.87% to 70.54 % with an average of 58.53% (Table 1). It can be concluded that the pore size greater than $R_{\rm f}$ makes the most contribution to the permeability. The samples exhibit various R_f values, indicating they are described with different pore structures. It should be noted that there is a negative relationship between R_f and P_{cd} . The larger the R_f is, the lower the $P_{\rm cd}$ is (Table 1). The lower threshold pressure indicates larger pores existing attributed to the mercury being easy to intrude into large

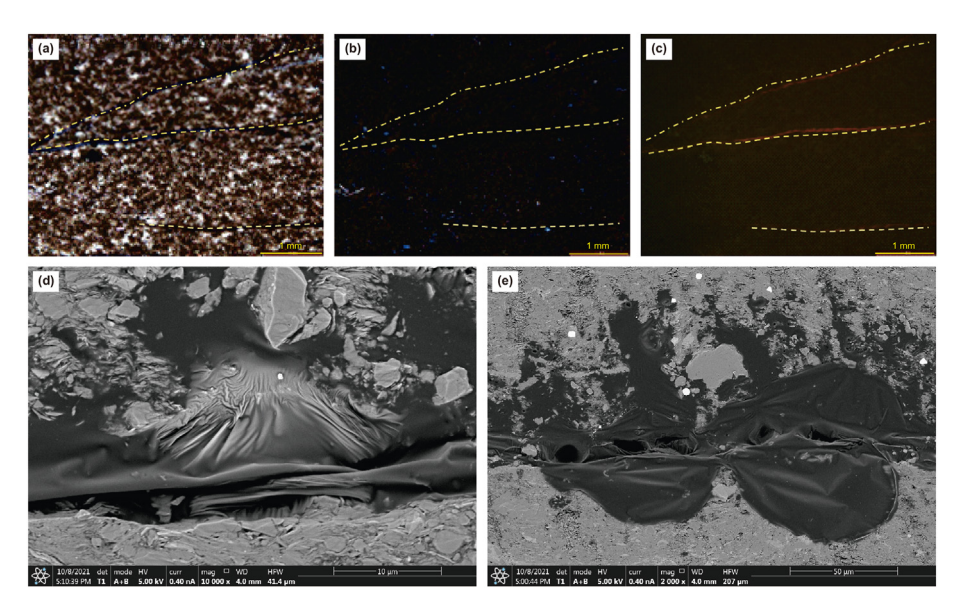


Fig. 5. Characteristics of oil accumulation observed through thin sections, fluorescent section, and SEM. (a), (b), and (c) exhibit the oil occurrence along lamellation fractures observed by microscope under plane-polarized, cross-polarized, and fluorescent light, respectively. Well Y, 2324.84 m. (d) and (e) display oil film observed by SEM, Well Z, 2497.1 m.

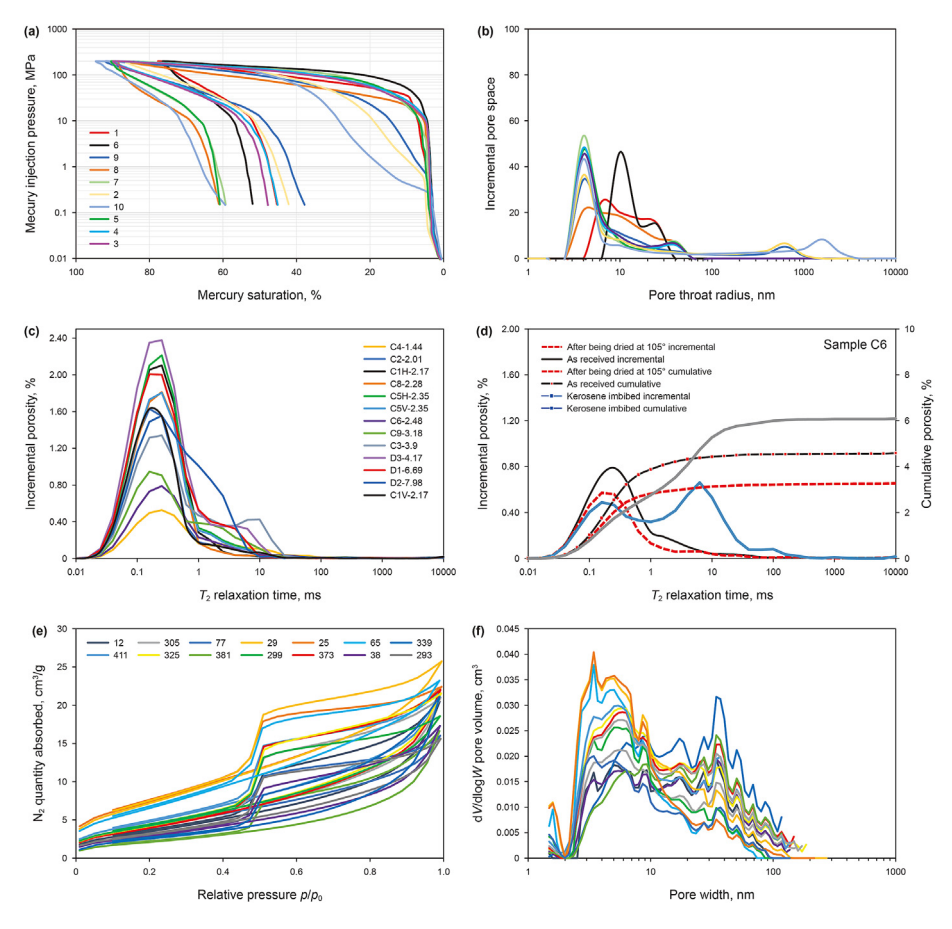


Fig. 6. Pore and throat characteristics were observed by MICP, NMR, and N_2 adsorption. (a) The mercury intrusion and withdrawal curves of samples from Well X and (b) the corresponding pore size distribution. (c) The NMR T_2 spectra of samples from Wells SS and WW. "C4-1.44" means sample C4 and its TOC content is 1.44%. (d) T_2 spectra of sample C6 under three conditions (AS, D, and KI). (e) and (f) The adsorption-desorption curves and pore size distribution of samples from Well X.

pores with lower pressure. Structure coefficient, sorting coefficient, and homogeneous coefficient are good indices for petrologic feature and pore structure analysis Thus, these parameters play

essential roles in pore structure classification and reservoir quality evaluation.

Characteristics of parameters derived from MICP.

Well	Samples	Strata	Depth, m	φ , %	$K_{\rm s}$ $10^{-3}~\mu{\rm m}^2$	Pore thi	Pore throat radius, µm	m,	Pore size distributio	on	Permeability distribution	bility tion	9-	D	B	Mercury saturation	turation	We, %	$P_{ m cd}$, MPa
						Ra	$R_{ m p}$	R ₅₀	R _v , μm	Rm, %	Rf, µm	Fm, %				SHg _{max} , %	S _r , %		
×	1	05	2554.76	3.974	0.010	0.021	0.008	0.007	900.0	20.040	0.016	55.137	0.033	94.970	0.384	77.530	45.313	41.554	34.445
×	2	62	2555.16	2.952	0.010	1.086	0.135	900'0	900'0	11.591	0.630	60.177	6.710	44.602	0.124	999.98	42.157	51.357	0.677
×	3	62	2556.16	4.629	0.010	0.053	0.010	900'0	900.0	17.467	0.040	56.121	0.064	109.418	0.196	89.771	47.788	46.766	13.768
×	4	62	2557.66	4.094	0.010	0.053	0.010	900'0	900.0	15.742	0.040	55.599	0.052	113.790	0.189	89.515	45.120	49.595	13.769
×	5	62	2558.16	6.275	0.010	0.053	0.009	900'0	900'0	19.980	0.040	61.775	990.0	114.559	0.172	90.357	60.880	32.623	13.772
×	9	07	2564.01	3.524	0.010	0.015	0.005	0.005	0.010	15.050	0.010	70.535	0.013	92.459	0.355	76.319	51.965	31.911	48.225
×	7	02	2565.61	4.661	0.010	0.053	0.009	900.0	900'0	14.255	0.040	64.739	0.051	115.593	0.176	90.549	59.285	34.527	13.769
×	8	05	2566.01	3.027	0.010	0.053	0.013	0.010	900'0	19.936	0.040	43.864	0.068	87.853	0.252	88.530	61.128	30.952	13.770
×	6	02	2566.41	3.908	0.010	1.087	0.112	0.008	900'0	16.348	0.630	61.453	6.146	88.056	0.103	91.889	37.834	58.826	9.676
×	10	02	2567.61	4.732	0.010	2.782	0.494	0.007	9000	8.525	1.600	55.859	144.595	11.120	0.178	94.456	59.407	37.106	0.264

is pore size and pore volume of the permeability peak, respectively, ϕ is structure coefficient. D represents sorting coefficient and α is homogeneous coefficient. SIg_{max} and S_r represent the maximum mercury intrusion saturation the residual mercury saturation, respectively. W_e is the maximum mercury withdrawal efficiency. P_{cd} is the threshold pressure.

3.2.2. NMR analysis results

The original NMR T_2 spectra of the tested shale samples are exhibited in Fig. 6(c). It can be seen that most spectra are characterized by unimodal behavior and some are bimodal with left-skewed. T_2 components are concentrated in short T_2 relaxation times (0.1–1 ms), indicating the pore space is dominated by micropores. Some spectra display a tail feature at long T_2 components (10–100 ms), which could result from microfractures and lamellation fractures.

Porosity obtained on the condition of being dried at 105 °C decreases as a whole of all samples (Table 2). However, the porosity varies difference on the state of kerosene saturated compared with that of the original state. T_2 spectra of samples under various test conditions change a lot. Taking C6 for example, T_2 spectrum in the original state behaved in unimodal, but changed into bimodal behavior with right-skewed, which indicates prior oil accumulation in large pores discharge during the drilling coring process. T_2 spectrum is characterized by unimodal and trimodal behaviors on the original state and kerosene imbibed state, respectively, implying complex pore-fractures systems (Fig. 6(d)). Notably, clay minerals have strong adsorption to kerosene and the mineral content is high in the Qingshankou Formation. Thus, the proton detected by NMR test consists of the proton generated by fluid saturated in pores and the hydrogen in hydrocarbon (kerosene) absorbed by clay minerals. The T_2 spectra of cores on the condition of kerosene imbibed is a common effect of physical saturation and chemical adsorption. Therefore, in this study, the kerosenesaturated samples are not used to characterize the pore structure and the original and dried samples are selected to depict the pore structure analysis.

3.2.3. N_2 adsorption analysis results

The N₂ adsorption experiment is best suited for investigation of materials with pores smaller than 300 nm (Anovitz and Cole, 2015), and the pore size of shales in the Qingshankou Formation in the Gulong Sag, Songliao Basin is in this range (Liu et al., 2019; Bai et al., 2022). The adsorption-desorption curves and pore size distribution of 14 tested samples are plotted in Fig. 6(e)–(f). The morphology of the adsorption and desorption curves as well as hysteresis loops behaviors of samples show various characteristics, demonstrating complex pore structure and strong heterogeneity. From the bottom to the top sorption curves of all these samples, the N₂ adsorption capacity increases gradually under lower relative pressure, implying the increasing extent of small pores (Fig. 6(e)-(f)) (Li et al., 2015). According to the IUPAC criteria, the dominant pore type is Type IV and the hysteresis loops are mainly characterized by H2 and H3 types (Figs. 1 and 6(e)). The maximum adsorption capacity of shales is in the range of 15.62-25.73 cm³/g, with an average of 19.92 cm³/g (Fig. 6(e)). The minimum adsorption volumes of shale range from 1 to 4.16 cm³/g, with a mean of 2.39 cm³/ g. The BET surface area, pore volume, and BJH average pore width are in the ranges of $8.07-27.98 \text{ m}^2/\text{g}$ (average value of $17.32 \text{ m}^2/\text{g}$), $0.02-0.04 \text{ cm}^3/\text{g}$ (mean value of 0.03 cm³/g), and 4.87–11.26 nm (mean of 6.69 nm), respectively (Table 3). The multiple peaks suggest complex pores composition, of which two main peaks are distributed at the ranges of 3-4 nm and 30-40 nm, indicating a high proportion of mesoporous (Fig. 6(f)). The pore size is mostly in 2-100 nm using N₂ adsorption technique, also implying the important contribution of micropores and mesopores (Fig. 6(f)).

3.2.4. CT analysis results

The 3D reconstructed images of shale samples using micro-CT are shown in Fig. 7. Grayscale images can be extracted during the data processing (Fig. 7(a) and (b)) (Wu et al., 2020; Gou et al., 2023). Following this, a two-phase segmentation method is applied to

Table 2Geochemical characteristics of samples tested in NMR experiment.

Well	Sample	Length, cm	Lithology	Depth, m	Porosity, %	P_{D}	P_{KI}	TOC, %	T _{max} , °C	S _{1,} mg/g	S ₂ , mg/g
SS	C-1	9	Shale	2150.65	7.91	3.04	6.77	2.12	420	5.81	8.23
SS	C-2	8	Shale	2142.15	7.91	3.04	7.44	1.91	413	7.67	7.75
SS	C-3	11	Shale	2134.39	9.01	5.69	10.75	3.70	448	10.46	19.77
SS	C-4	9	Shelly shale	2132.64	3.59	3.02	3.63	1.36	447	4.95	4.90
SS	C-5	8	Shale	2126.89	9.33	3.48	7.89	2.23	440	7.96	11.71
SS	C-6	8	Siltsandstone	2115.39	4.58	3.28	6.09	2.39	447	7.00	13.09
SS	C-8	12	Shale	2106.09	8.67	3.47	7.47	2.08	445	4.13	8.98
SS	C-9	7.5	Shale	2088.09	6.09	5.11	7.61	3.08	444	10.51	21.38
WW	D-1	5	Shale	2034.88	11.39	9.76	6.63	6.67	453	6.61	70.90
WW	D-2	5	Shale	2036.42	10.84	10.82	9.36	7.87	445	15.15	77.79
WW	D-3	5	Shale	2036.72	13.35	9.54	6.57	4.01	447	7.25	34.22

Porosity, P_D , and P_{KI} are the porosity detected under the original state, drying, and kerosene-imbibed conditions, respectively.

Table 3Pore features are described by N₂ adsorption

Well	Sample	Depth, m	TOC, %	Surface aera,	m ² /g	Pore volume,	cm³/g	Pore size, nm	ı
				Original	KI	Original	KI	Original	KI
Z	381	2505.1	3.21	8.0707	29.5981	0.025752	0.041967	10.6241	6.2949
Z	339	2484.1		9.706	36.7248	0.032729	0.054618	11.2592	6.5191
Z	241	2435.05		10.977	26.5844	0.025092	0.035327	7.4972	5.7365
Z	38	2333.6		11.3493	28.7879	0.026751	0.038091	8.3012	5.9264
Z	293			12.129	26.2576	0.02417	0.03244	7.0023	5.4826
Z	12			13.626		0.031697		8.1087	
Z	69	2349.1		13.9971	28.6511	0.02687	0.035563	6.8875	5.4992
Z	53	2341.09		14.4951	22.2068	0.025194	0.029426	6.3059	5.6612
Z	41	2335.1		14.5603	34.1586	0.031799	0.044454	7.4833	4.826
Z	45	2337.1		14.8394	22.9424	0.028222	0.03085	6.9191	5.952
Z	253			14.9561	26.1922	0.02728	0.03577	6.5322	5.8395
Z	373	2501.5	2.65	15.422	37.5257	0.034048	0.046624	7.5559	5.5071
Z	77	2353.1		15.5899	25.0013	0.024775	0.029635	5.9267	4.5493
Z	305			15.7416	33.4891	0.032507	0.04324	7.2413	5.6895
Z	299	2464.1	3.04	16.20	33.2266	0.028742	0.041491	6.317	5.4722
Z	33	2333.1		16.4169	27.6589	0.030172	0.03719	6.7236	5.9663
Z	49	2339.1		16.5297	32.6461	0.030989	0.039591	6.8603	5.4983
Z	325		2.71	16.6262	35.4489	0.033208	0.045567	7.0213	5.0058
Z	9	2319.1		17.2526	28.5691	0.030329	0.036072	6.2258	5.591
Z	22	2323.6		18.2567	29.7819	0.031074	0.036857	6.0919	5.4349
Z	411	2520.1	3.03	18.4334	37.2646	0.03386	0.04645	6.635	5.588
Z	257			18.7631	30.27	0.036479	0.042828	6.851	5.7185
Z	61	2345.1		19.4113	28.266	0.028712	0.033507	5.5975	5.2342
Z	153	2391.2		19.7756	37.256	0.032121	0.043418	6.0036	5.228
Z	57	2343.1		20.2806	29.673	0.030506	0.035593	5.1014	4.5786
Z	5			20.3767	30.1474	0.031456	0.036551	5.8737	5.3623
Z	317	2473.23		20.86	37.5529	0.034243	0.044548	5.9168	5.3168
Z	73	2351.1		21.1844	36.4733	0.03363	0.041367	5.9212	5.0516
Z	18			22.5306	28.8533	0.032558	0.035597	5.6899	4.7417
Z	125			22.7375	37.0357	0.031076	0.041029	5.2284	4.8098
Z	65	2347.1		25.5095	40.7876	0.035887	0.046016	5.2856	5.0411
Z	29			27.1315	38.0762	0.039799	0.042337	4.8958	4.9998
Z	25	2327.1		27.9768	30.9324	0.034664	0.037201	4.8715	4.794

separate pores and minerals phases according to the gray level threshold (Gou et al., 2023). The pore and throat, therefore, can be extracted and the ball-and-stick model as well as the connectivity model can be established (Fig. 7(c)–(f)). The positions, areas, volumes, and connectivity of pores and throats and fractures can be visualized from the 3D images (Fig. 7). It can be seen that the pores are characterized by elongated and irregular geometries and most pores are independent of each other. Although the pore volume seems big, the connectivity of pores is poor, demonstrating complex pore networks, which brings an enormous challenge for oil recovery (Fig. 7(f)). In the area away from the fractures, rarely colors can be seen (Fig. 7(e) and (f)). However, there is a wide area of the same color distribution along the fractures, suggesting that the connectivity can be good, implying that the development of

fracture can enhance the connection between pores and throats, and thus, significantly improve the reservoir quality (Fig. 7(f)).

Due to the fact that micro-CT provides access to a limited range of scales, the smaller pores (nano-scale pores) can not be detected. However, the CT scanning takes advantage of displaying visible information about pore/fracture system's spatial position and their relationships. The pore size distribution and characteristics are in agreement with those revealed by SEM, MICP, NMR, and N_2 sorption, which indicates that all of these experiments can verify and complement each other. Combining CT with other techniques, such as MICP, NMR, and N_2 adsorption, is therefore suitable for characterizing the pore structure of shales, of which the nano-scale pores are dominant.

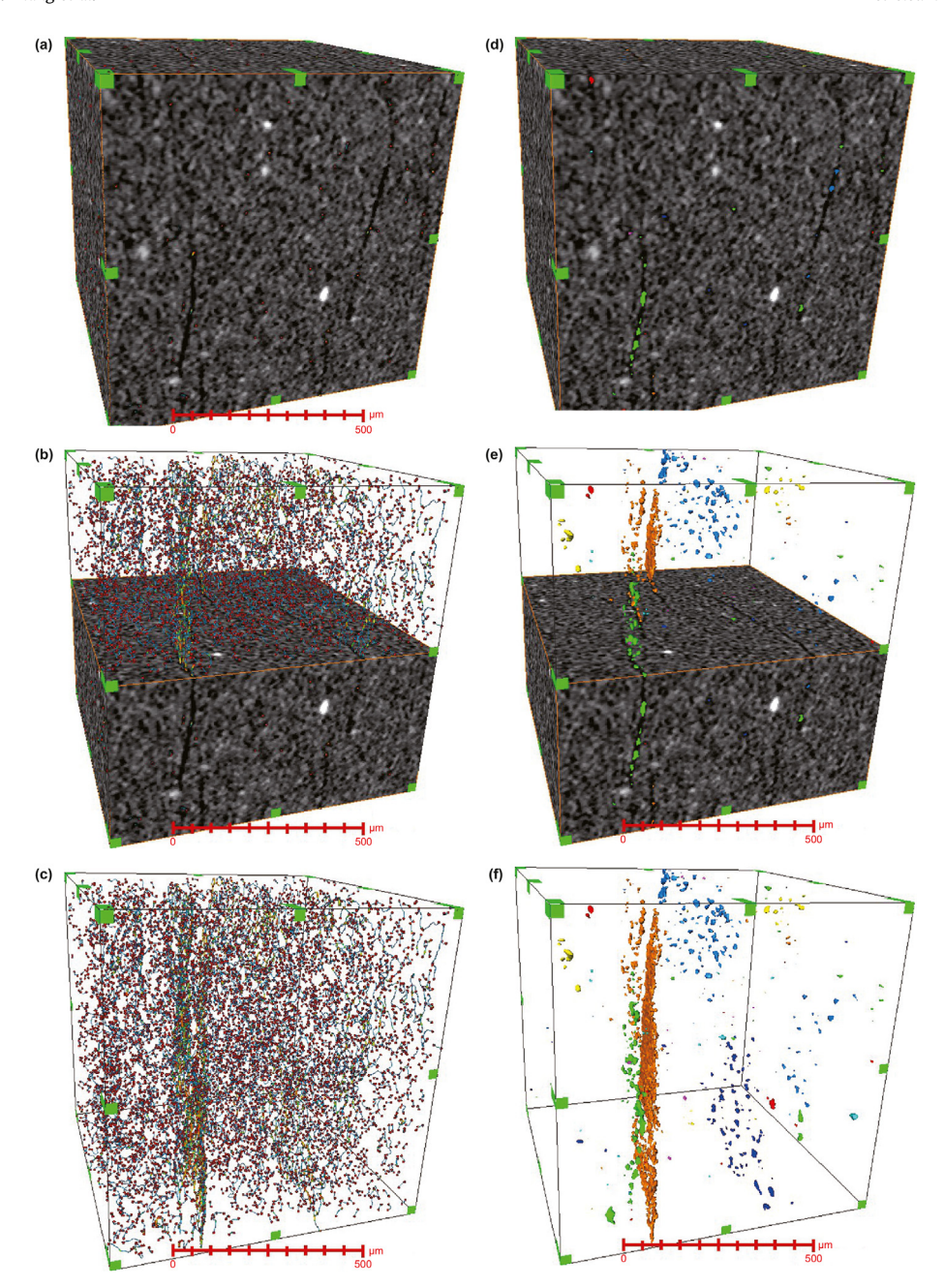


Fig. 7. The results of micro-CT and pore network reconstruction, Well X, 2548.76 m. (a) Reconstructed grayscale volume with pores and throats bodies. (b) Segmented of half ball-and-stick model and half grayscale volume. (c) The ball-and-stick model of pore and throat. (d) Reconstructed grayscale volume with connectivity bodies. (e) Segmented of half connecting body model and half grayscale volume. (f) The connecting body model. The same color represents connected pores. Otherwise, it indicates that the pores/fractures are independent of each other.

4. Discussion

4.1. Pore structures classification

4.1.1. Pore structure characteristics according to MICP

Three types of pore structures are divided according to the shape of intrusion-extrusion curves and capillary parameters.

Type I pore structure is characterized by the lowest threshold pressure (0.264 MPa), the higher mercury withdrawal efficiency (37.106%), the highest mercury injection saturation (94.456%), the highest $R_{\rm f}$ (1.6 μ m), and the largest pore throat radius ($R_{\rm a} = 2.782~\mu$ m and $R_{\rm p} = 0.494~\mu$ m), with both ends and open pores

as well as ink-bottle-shapes pores (Figs. 1 and 8(a), Table 1). The reservoir space is mainly composed of nano-pores (organic pores and intercrystalline pores) and microfractures or lamellation fractures (Fig. 8(a)). According to XRD data analysis, the reservoir is dominated by laminated felsic shales or clay shales (Fig. 8(a)).

Type II pore structure is characterized by moderate threshold pressure (13.769 MPa), medium mercury withdrawal efficiency (34.527%), moderate mercury injection saturation (90.549%), moderate $R_{\rm f}$ (0.040 μ m), and moderate pore throat radius ($R_{\rm a}=0.053~\mu{\rm m}$ and $R_{\rm p}=0.009~\mu{\rm m}$), with ink-bottle-shaped pores and slit-shaped pores (Figs. 1 and 8(b)—Table 1). The reservoir space is dominated by intragranular dissolution pores, intercrystallite and

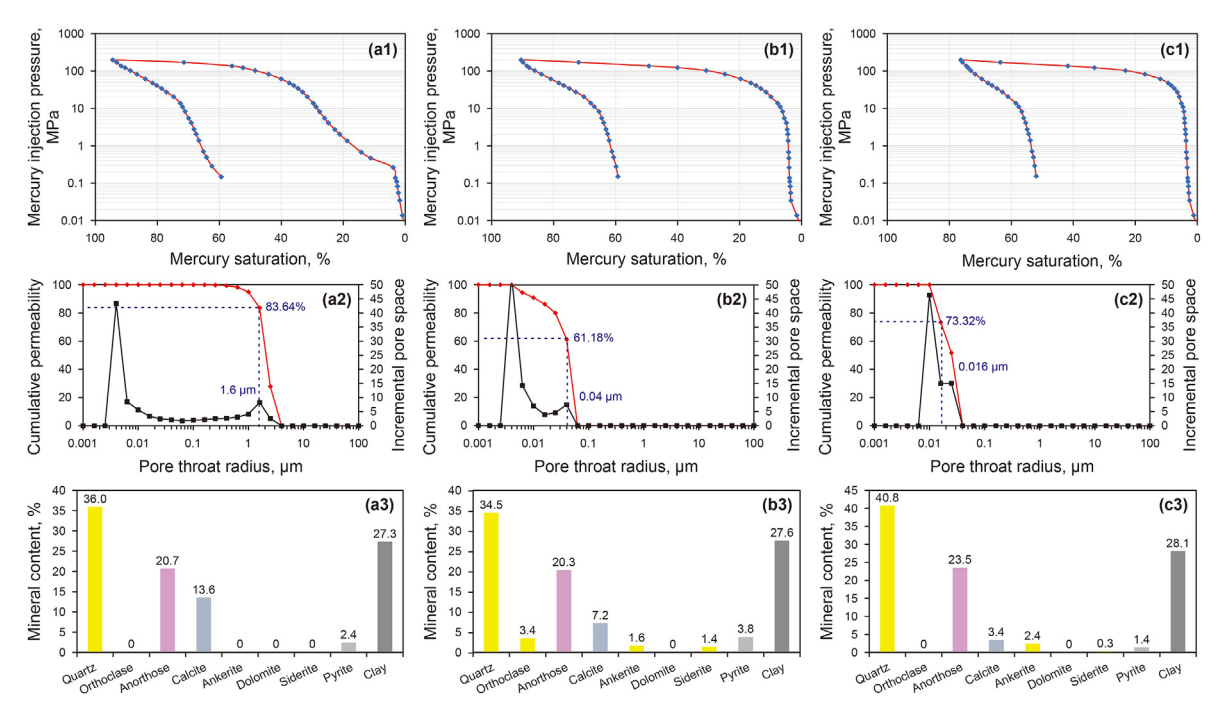


Fig. 8. Typical MICP curves and XRD characteristics of three pore structure types for shale in the Qingshankou Formation. These three typical samples are highlighted in Table 1. (a) The intrusion-extrusion curves (a1), pore size distribution and cumulative permeability curve (a2), and mineral composition of Type I pore structure (a3). Sample 10, TOC = 1.03%. (b) Type II pore structure, Sample 7, TOC = 1.09%. (c) Type III pore structure, Sample 6, TOC = 1.87%.

intracrystalline pores, and organic pores. This type of pore structure is commonly observed in layered felsic shales and clay shales (Fig. 8(b)).

Type III pore structure shows the following features: the highest threshold pressure (48.225 MPa), the lowest mercury withdrawal efficiency (31.911%), the lowest mercury injection saturation (76.319%), the lowest $R_{\rm f}$ (0.010 μ m), and the smallest pore throat radius ($R_{\rm a}=0.015~\mu$ m and $R_{\rm p}=0.005~\mu$ m), with slit-shaped pores and narrow slit-like pores (Figs. 1 and 8(c)—Table 1). The dominant pore spaces are nano-scale organic pores or barely pores.

From type I to type III, the threshold pressure increases, while W_e , SHg_{max} , R_f , R_a , and R_p decrease. These three typical samples show similar mineral compositions and TOC content, especially Samples 10 and 7, but express different pore structures, implying strong heterogeneity and complex mechanisms.

4.1.2. Pore structure characteristics according to NMR

NMR T_2 spectra of shales are categorized into three types: bimodal (Type I), unimodal (Type II), and unimodal with low amplitude (Type III), which corresponds to the MICP classification. The different T_2 spectra and T_1 - T_2 maps directly reflect various kinds of pore systems and occurrence states.

Type I pore structure is characterized by bimodal behavior with a major left peak and a weaker right peak, implying two pore size populations are present and microscale pores and throats are dominant (Fig. 9(a) and (b)). The lithology is shale estimated by XRD (Fig. 9(c)). The signal intensity decreases on the condition of being dried, indicating both clay bound water and irreducible water in micropore and mesoporous disappear (Fig. 9(d) and (e)). From the core observation, lamellation and intersected high-angle natural fractures can be seen, which can explain the longer T_2 (>100 ms) component relaxation time response after kerosene was imbibed (Fig. 9(a) and (d)–(f)). The total porosity obtained from the cumulative curve is high up to 9.01% (Table 2), indicating this type of pore structure is favorable for high quality reservoirs.

Type II pore structure exhibits unimodal behavior with leftskewed, indicating rare occurrences of macropores (Fig. 9(g)–(h)). The lithology is also defined as shale according to XRD analysis (Fig. 9(i)). The higher amplitude of short T_2 components represents a large number of micropores including intragranular dissolution pores, intercrystalline pores developed in clay minerals or clay mineral aggregates, and organic pores (Fig. 9(h)). The T_1 - T_2 maps of three different conditions display the fluid occurrence states in these pores (Fig. 9(j)-(1)). Compared with the original state, after being dried, the signal intensity of the cluster at the lower-left corner decreases indicating irreducible water and clay bound water accumulated in micropores (short T_2 components) evaporate at high temperatures (Fig. 9(j) and (k)). On the condition of kerosene imbibed, all signal grows strong and new signals of cluster located at the upper-right corner appear (Fig. 9(1)). This may be explained by the loss of prior oil in connective larger pores and throats during the process of coring. The signal intensity of this cluster is weaker than that of type I indicating the volume of large pores in type II is less than that in type I. Additionally, the porosity obtained from the cumulative curves is lower (Table 2). Therefore, the reservoir quality of this type of pore structure is fair.

Type III pore structure also exhibits unimodal behavior, but the height of the peak is different from Type II (Fig. 9(m), (n)). The amplitude of this type is lower than that of type II, implying a smaller pore volume, which can be verified by the porosity data (Table 2). The short T_2 components represent a narrow distribution of discontinuous nano- and micro-scale pores. The XRD analysis illustrates that the lithology is also shale but with less clay content (Fig. 9(o)). The T_1 - T_2 maps obtained from three states show similar features to that of type II, but the signal intensity is weaker, indicating smaller pores and disconnected pores and throats (Fig. 9(p)—9(r)).

Although the mineral compositions of three typical pore structure samples exhibit similar characteristics, the structure of rocks and physical properties are quite different (Fig. 9(c), (i), (o), Table 2).

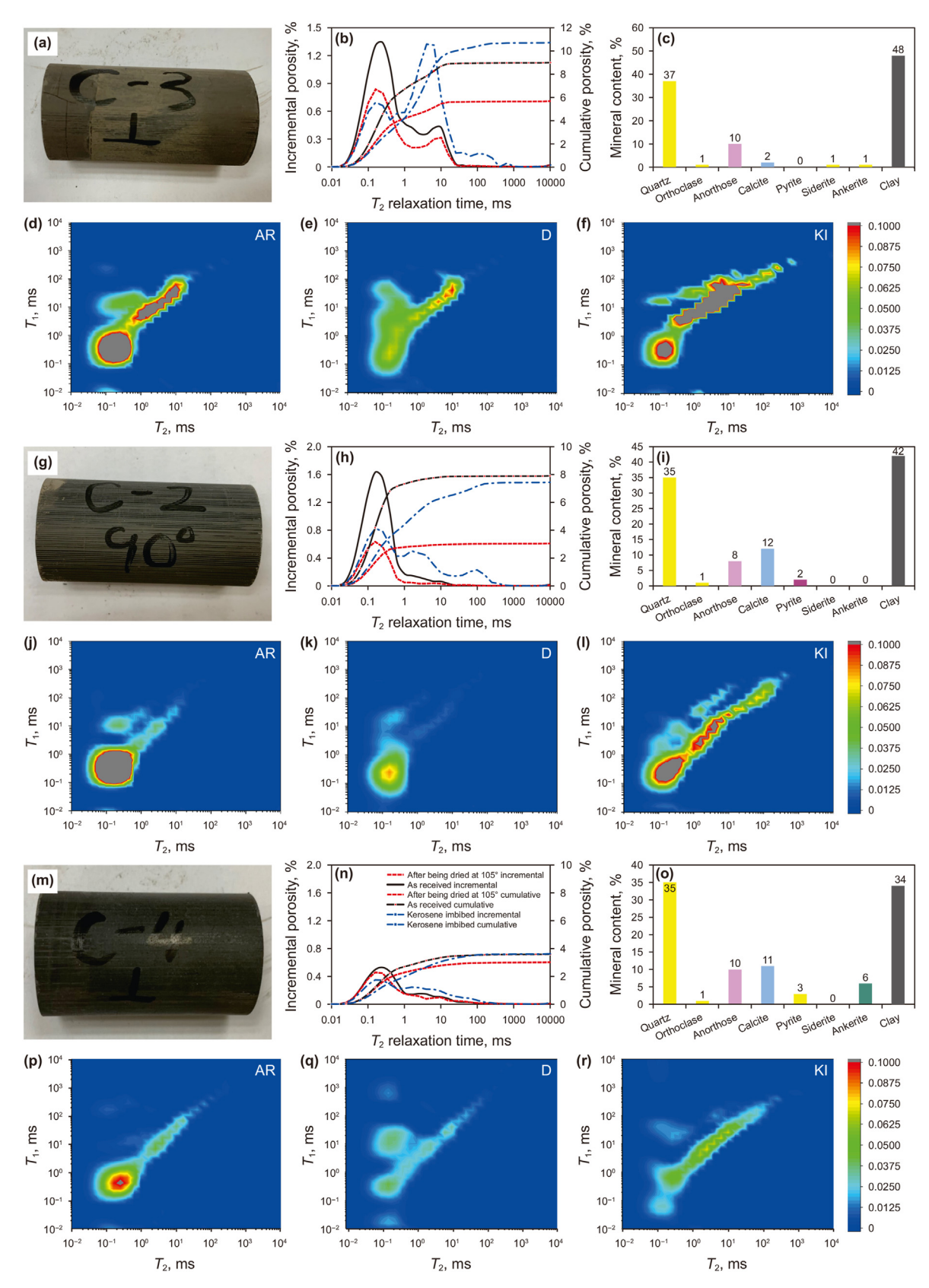


Fig. 9. Three pore structure types are classified by NMR. These three typical samples are marked in Table 2.(a)—(f) Type I pore structure demonstrated by core photo (C3, TOC = 3.70%), NMR T_2 distribution, mineral content, 2D-NMR T_1 - T_2 maps on the conditions of AS, D, and KI, respectively. (g)—(I) Type II pore structure demonstrated by core photo (C2, TOC = 1.91%), NMR T_2 distribution, mineral content, 2D-NMR T_1 - T_2 maps on the conditions of AS, D, and KI, respectively. (m)—(r) Type III pore structure demonstrated by core photo (C4, TOC = 1.36%), NMR T_2 distribution, mineral content, 2D-NMR T_1 - T_2 maps on the conditions of AS, D, and KI, respectively.

The reason may be the rocks' deformation controlled by thermal evolution degree and diagenesis during burial history (Table 2). The T_2 spectra display unimodal and bimodal behavior on the original state and dried state and exhibit trimodal and multimodal distribution on the kerosene imbibed state, indicating a complicated geometric arrangement and strong heterogeneity in shales. The NMR test provides more pore bodies and discontinuous pores information, especially micropores (short T_2 components) than MICP. Thus, the porosity detected by NMR test is larger than that obtained by MICP experiment (Tables 1 and 2).

4.1.3. Pore structure characteristics according to N_2 adsorption

The morphology of isotherms and their hysteresis patterns provide information about the shape and volume of pores, which have an effect on the physisorption mechanism (capillary condensation) (Thommes et al., 2015; Gou et al., 2023). According to the shape of the adsorption-desorption curve, the hysteresis loops, and parameters derived from gas adsorption, including surface area, pore volume, and average pore size, the pore structure is divided into three types.

Type I pore structure exhibits the largest average pore size and the lowest surface area and pore volume (Fig. 10). When the relative pressure is approximately 0.45, the desorption curve gets away from the adsorption curve dramatically, which is similar to H2. While, at the relative pressure of 1, the desorption curve increases rapidly without adsorption saturation, the feature of which is quite similar to type H3 (Figs. 1, 10(a) and 10(c), 10(e)). Therefore, the hysteresis loop is a mixture of type H2 and H3, corresponding to the composition of ink-bottle-shaped pores and slit-shaped pores (Figs. 1, 10(a) and 10(c), 10(e)). According to BET and BJH models, the surface area is 8.0707 cm²/g, the pore volume is 0.02575 cm³/g, and

the average pore diameter is 10.6241 nm (Table 3). It also can be seen from the pore size distribution plot, that the main peak of pore volume is distributed at 35–45 nm, indicating the pore size is relatively larger (Fig. 10(b)). This kind of pore structure provides the largest space for oil accumulation and the oil can easily immigrate due to the smallest surface area (Zhao et al., 2023).

Type II pore structure: the specific surface area, pore volume, and average pore size of the typical sample are 16.20, 0.02874, and 6.313 nm, respectively (Table 3). The hysteresis loop exhibits a little difference from that of type I. At the high relative pressure, the curve varies steadily (Fig. 10(c)), which means no open pores or micro fractures and lamellation fractures (Gou et al., 2019). The pore size distribution curve shows that most pore size is in the range of 3-20 nm, which is smaller than that of type I (Fig. 10(d)).

Type III pore structure shows similar features to type II, but is poorer than type II. The isotherm plot and hysteresis loop suggest that the dominant pores are ink-bottle- and slit-shaped pores (Fig. 10(e)). The pores ranging from 3 to 10 nm make a significant contribution to the pore space (Fig. 10(f)), indicating the most proportion of pores are isolated organic pores and intracrystalline pores. This type of pore structure is characterized by the highest surface area (27.1315 cm²/g) and the smallest average pore width (4.8958 nm) (Table 3). Shale characterized by pore structure III is thought to absorb more oil generated by organic matter due to its greater surface area (Zhao et al., 2023). In addition, only a small number of isolated and small pores are hosted in shales characterized by type of pore structure III. Therefore, oil can not be charged into or expelled from these rocks.

4.1.4. Pore structure characteristics according to CT The resolution of micro-CT is too low to effectively identify the

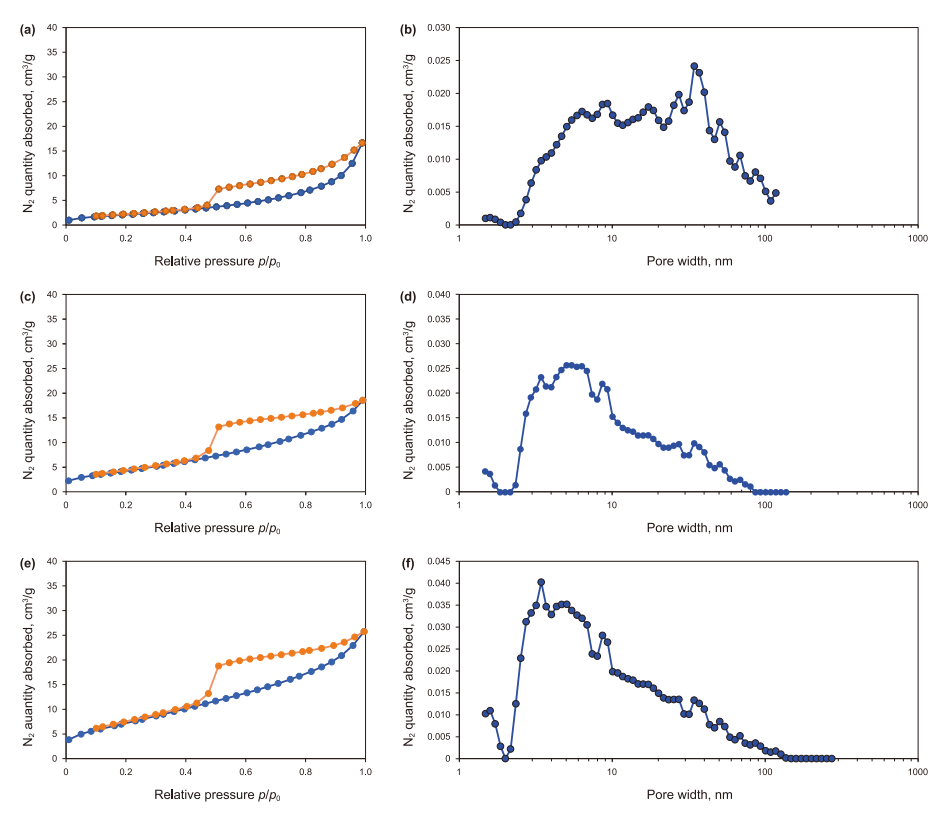


Fig. 10. Three pore structure types are divided by N_2 adsorption. (a) Type I pore structure, surface area is 8.0707 cm²/g, pore volume is 0.02575 cm³/g, and average pore diameter is 10.6241 nm, Well Z, 2505.1 m. (b) The corresponding pore width distribution curve of (a). (c) Type II pore structure, surface area is 16.20 cm²/g, pore volume is 0.02874 cm³/g, and average pore diameter is 6.313 nm, Well Z, 2429.13 m. (d) The corresponding pore width distribution curve of (c). (e) Type III pore structure, surface area is 27.1315 cm²/g, pore volume is 0.03980 cm³/g, and average pore diameter is 27.1315 nm, Well Z, 2329.15 m. (f) The corresponding pore width distribution curve of (e).

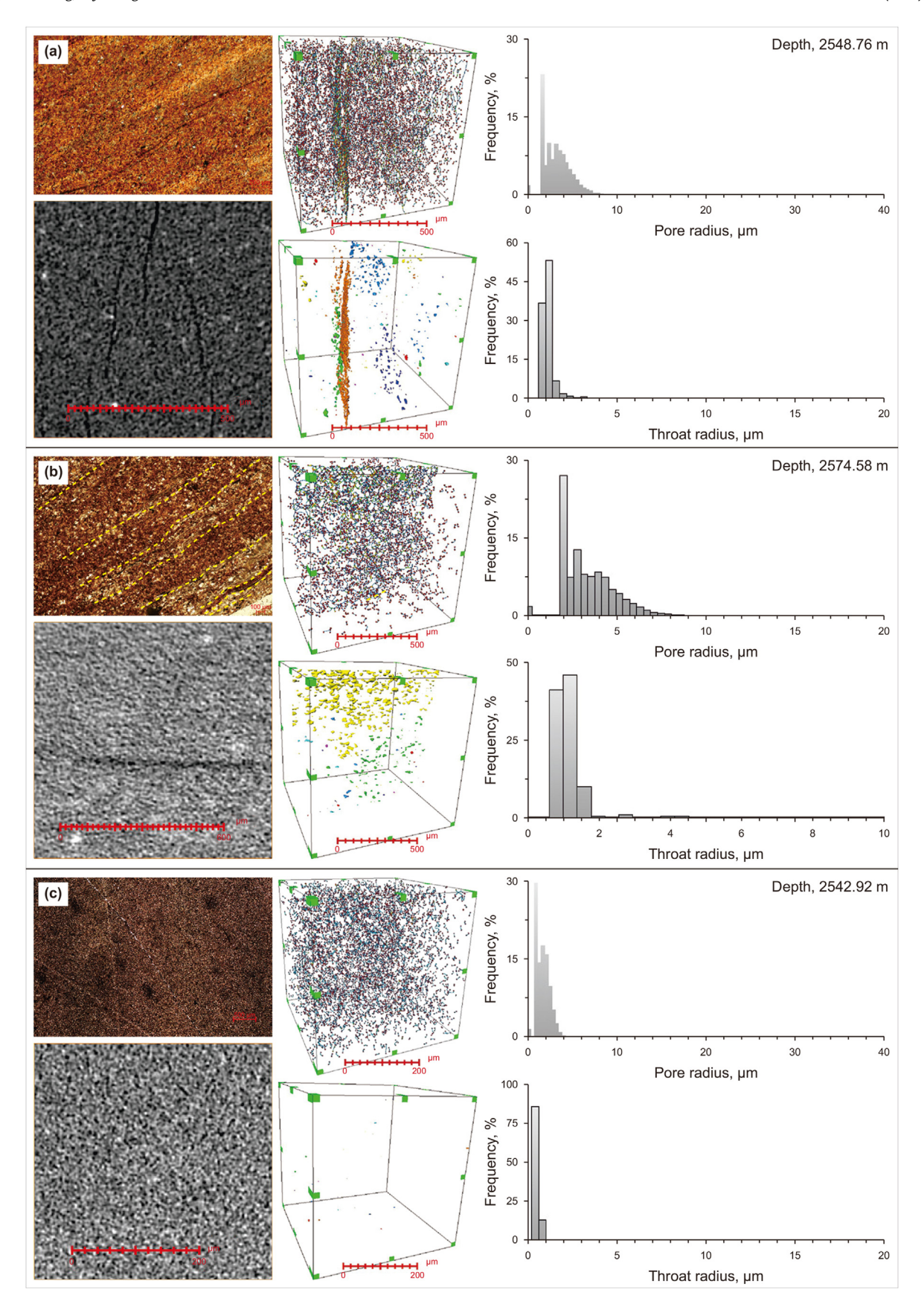


Fig. 11. Characteristics of three pore structures observed through CT. (a) Type I pore structure, Well X, 2548.76 m. (b) Type II pore structure, Well X, 2574.58 m. (c) Type III pore structure, Well X, 2542.92 m.

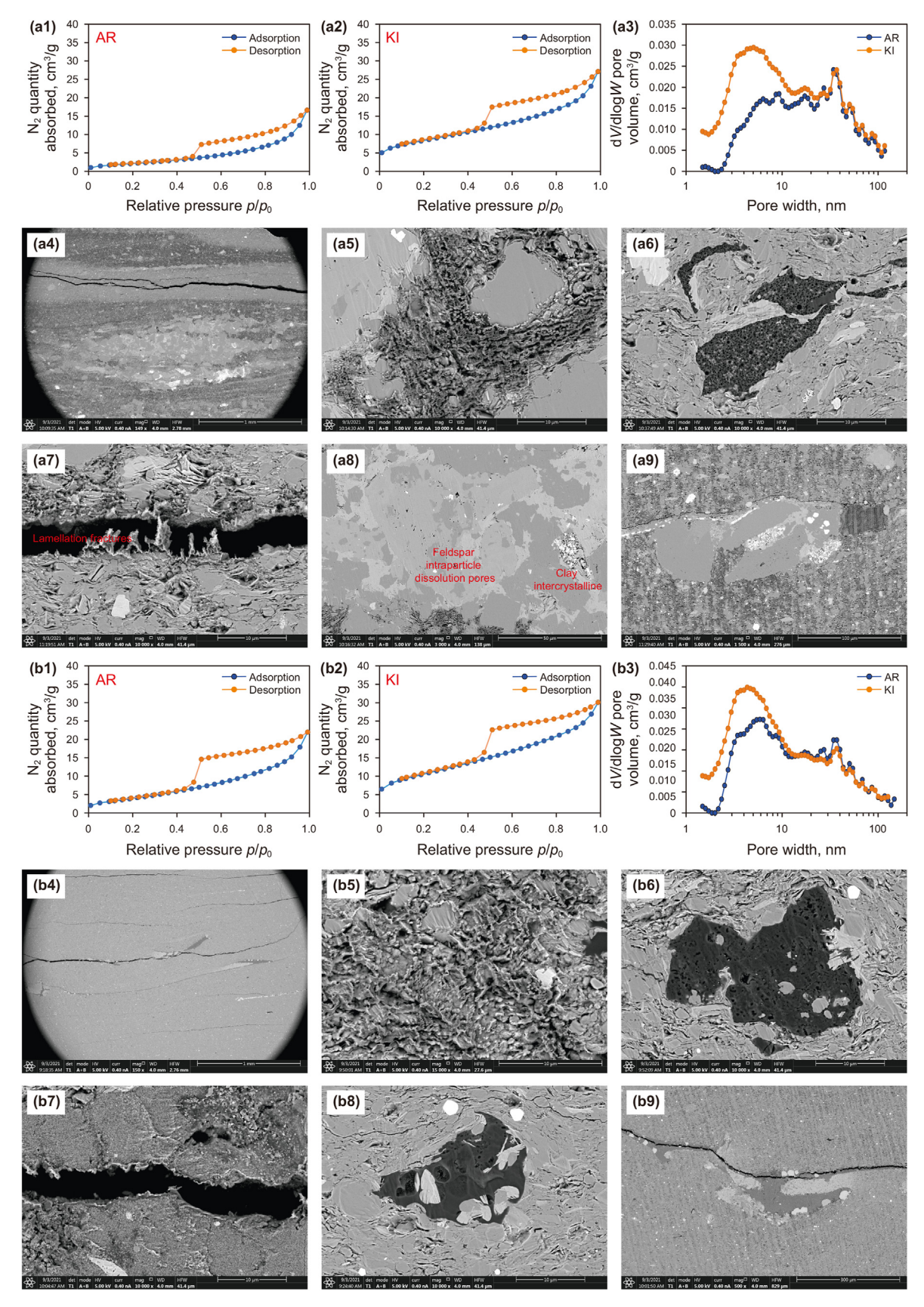


Fig. 12. Characteristics of pore types and thermal evolution degree of Type I pore structure. (a) and (b) are Samples 381 and 373, respectively. These two are highlighted in orange background in Table 3.

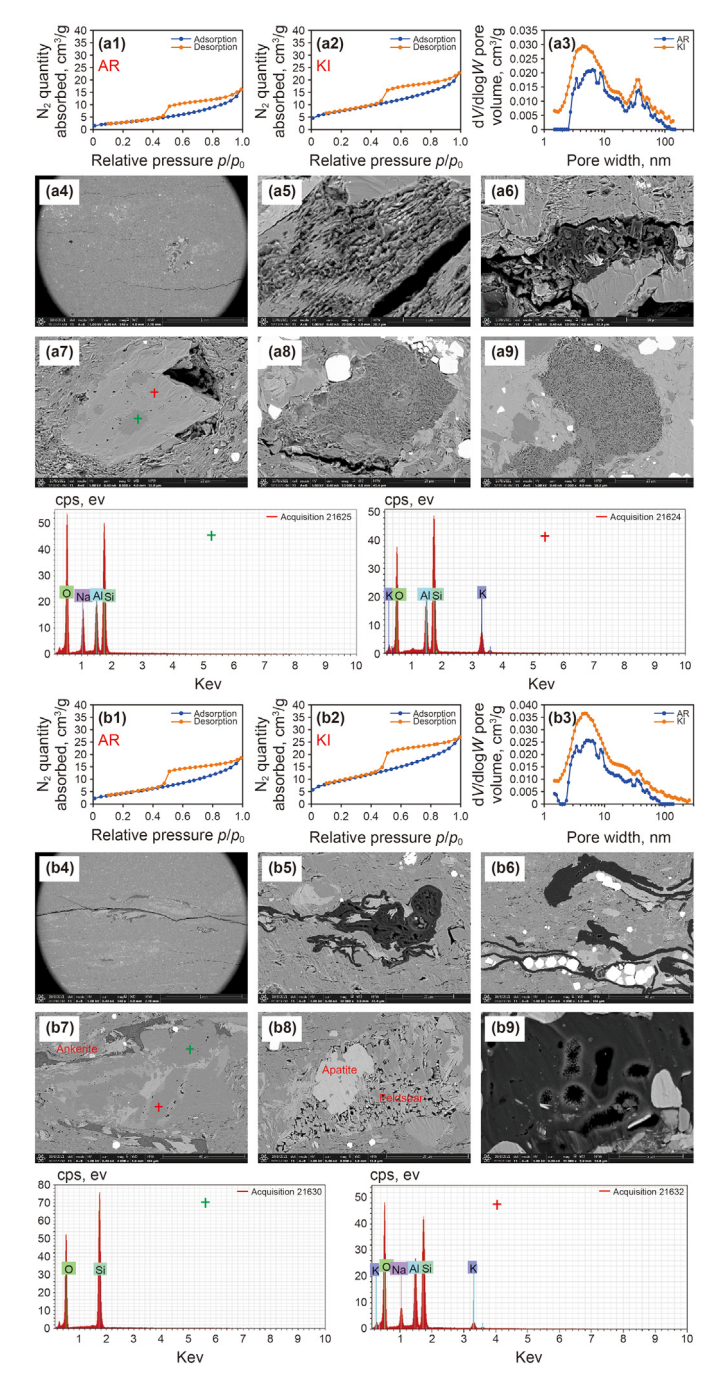


Fig. 13. Characteristics of pore types and thermal evolution degree of Type II pore structure.

(a) and (b) are Samples 241 and 299, respectively. These two are highlighted in yellow background in Table 3.

micropores. However, the reconstructed visualized 3D images show the pores/fractures system clearly. According to the ball-and-stick model and pore and throat distributions, three types of pore structure are divided as shown in Fig. 11.

Type I pore structure is characterized by more pore volumes and lamellation fractures occurring along the lamina can be seen on the thin section (Fig. 11(a)). More connected bodies appear along the fracture surface suggesting that the lamellation fractures play an essential role in reservoir quality (Fig. 11(a)). The pore and throat size distribution show that the pore size ranges from 1 to 8 μ m, and

is concentrated in 2–5 μ m (Fig. 11(a)). The throat is distributed in 0.6–2 μ m (Fig. 11(a)).

Type II pore structure is characterized by laminated structure in shales (Fig. 11(b)). Abundant pores can be observed in the ball-and-stick model but the position of the same color of adjacent pores is dispersed, indicating the connectivity of pore networks is poorer than type I (Fig. 11(b)). The pore radius size ranges from 2 to 7 μ m, mainly distributing in 2–4 μ m, and the peak is located at 2 μ m, which is the same as type I (Fig. 11(b)). The throat radius is distributed in the range of 0.6–1.6 μ m, which is smaller than type I (Fig. 11(b)).

Type III pore structure also exhibits abundant pores in the ball-and-stick model but no obvious laminae and fractures in thin section (Fig. 11(c)). The connectivity body model show rarely colors suggesting these pores are independent from each other (Fig. 11(c)). The pore size and throat size are in $1-4~\mu m$ and $0-1~\mu m$, respectively, indicating smaller pore space than type II (Fig. 11(c)).

From type I to type III, the content of adjacent pores decreases and the pore and throat size become smaller. Therefore, type I corresponds to high reservoir quality, and type III is developed in poor reservoir quality. The pore structure classification is in agreement with those revealed by MICP, NMR, and N2 adsorption, and CT scanning, implying that all of these tests can verify and complement each other. The reservoir characterized by type I pore structure exhibits favorable physical properties, such as high porosity and lamellation fractures development. The pore types are dominated by organic pores, intercrystalline pores and intraparticle dissolution pores in type II pore structures. Some of these pores can be connected by narrow throats or microfractures. The pores, developed in type III, are mainly intercrystalline pores and intraparticle pores, which are isolative and invalid.

4.2. Characteristics of different pore structures

Multiple laboratory techniques are used to characterize the multi-scale pore structure of shale, including SEM, MICP, N2 adsorption-desorption, CT scanning, NMR, and 2D NMR. Especially 2D NMR is favorable for the determination of fluid types and contents. Three types of pore structure are classified according to the pore size distribution, pore and throat connection, and reservoir space types. CT scanning provides a 3D visualization of reservoir space and directly shows the relationship between pores and throats and the characteristics of fractures. Of all of these experiments, N2 adsorption exhibits the best in characterizing pores in shales due to its high resolution for the assessment of nano-scale pores. MICP and NMR have a better advantage in characterizing pore space of sandstone reservoirs, even tight sandstone reservoirs. Additionally, the N2 adsorption and desorption under different states are helpful for hydrocarbon accumulation evaluation.

After extraction, the total pore volume of Type I and II pore structures increased significantly, while that of Type III shale samples remained almost unchanged (Figs. 12–14). Type I is correlated with hydrocarbon generation expulsion, and migration, while type II is not.

Type I pore structure: this type of pore structure developed in reservoirs characterized by a high degree of thermal evolution. Previous oil and gas generated by kerogen have been discharged and incharged into adjacent reservoirs. The hysteresis loop exhibited the same the morphology and type before and after extraction, indicating the characteristics of pore and throats didn't change (Fig. 12(a1), 12(a2), 12(b1) and 12 (b2)). However, the volume of nano-pores increased after extraction compared with the received sample (Fig. 12(a3) and 12 (b3)). Notably, the pore size distribution of macropores remained unchanged, which can be explained by the adsorption of clay minerals (Fig. 12(a3) and 12

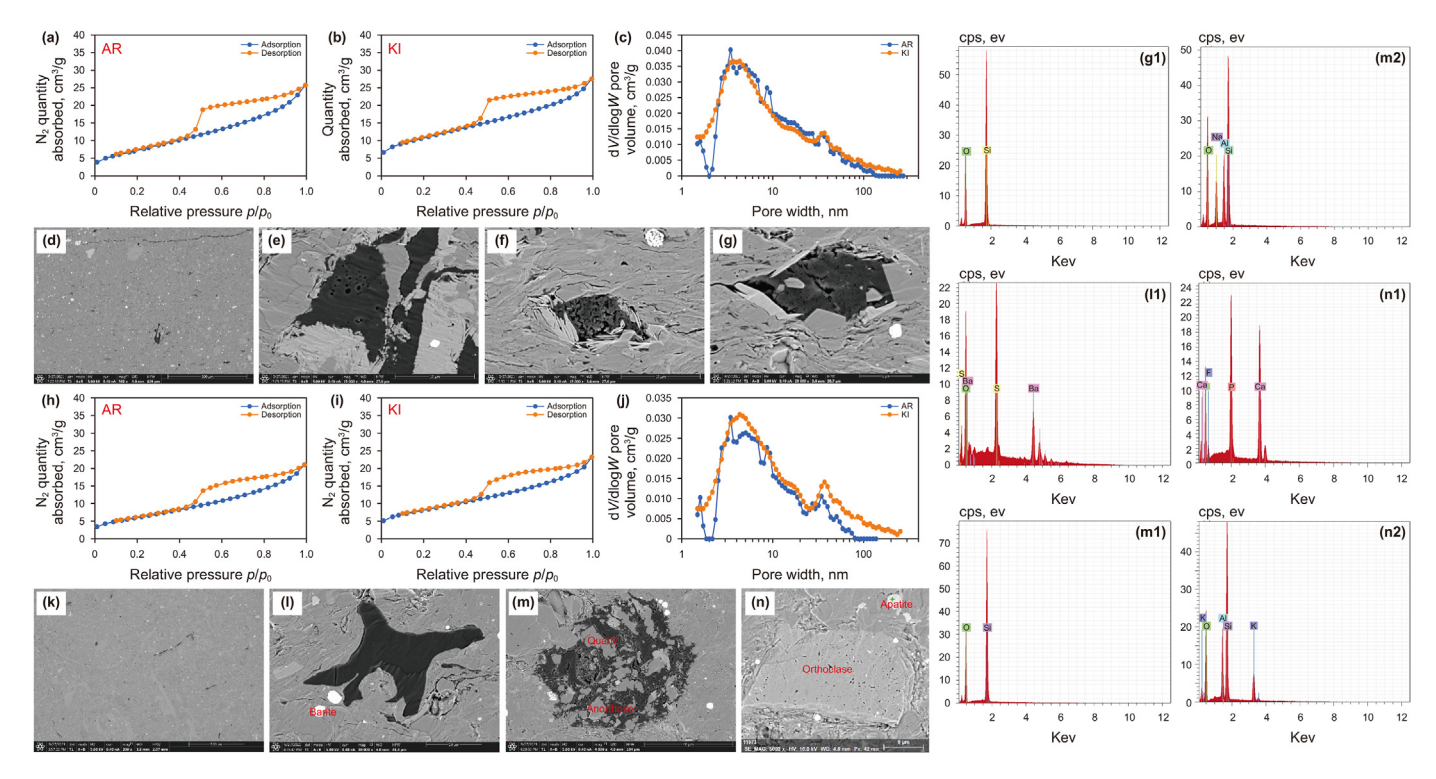


Fig. 14. Characteristics of pore types and thermal evolution degree of Type III pore structure. (a)—(g) is Sample 29 and (h)—(n) represents Sample 18. These two are highlighted in gray background in Table 3.

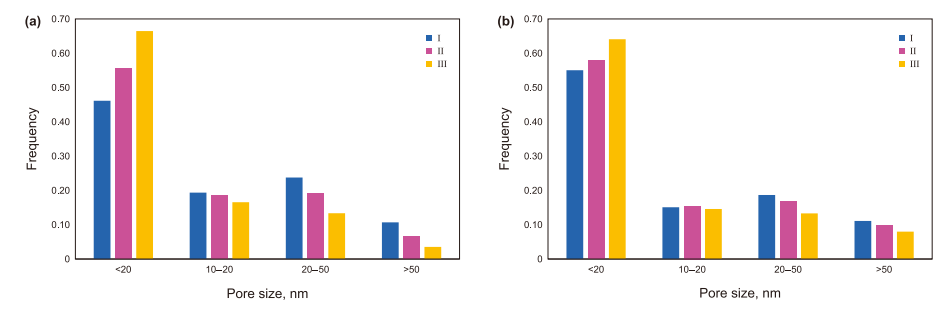


Fig. 15. Frequency histogram of different pore sizes of three pore structure types. (a) Is as received and (b) is after being extracted by methylene chloride.

(b3)). The dominant pores are determined by organic matter pores and clay intercrystallite. From the SEM observation, micro-fractures can be recognized, and the organic matter pores and clay intercrystallite were observed (Fig. 12(a4)–(a9) and 12 (b4)–(b9)). The spongy and network organic pores characterized by spongy were formed by the hydrocarbon generation and emergent low-carbon hydrocarbon (Fig. 12(a6), 12 (b6) and 12 (b8)). In addition, the curves distributed with large pores, not overlapping before and after extraction, witness the resource migration (Fig. 12(a3) and 12 (b3)).

Type II pore structure: compared with type I, this type of pore structure appeared in reservoirs characterized by a relatively low degree of thermal evolution in which the oil and gas have been hosting without migration. The type of hysteresis loop remained unchanged on the original state and imbibed state (Fig. 13(a1), 13(a2), 13(b1), and 13 (b2)). The amplitude of pore size distribution increased after the samples were imbibed with methylene dichloride (Fig. 13(a3) and 13 (b3)). Lamellation fractures can also be seen in this type of pore structure (Fig. 13(a4) and 13 (b4)). Compared with the type I pore structure, the incremental volume

of macropores implied that there was oil hosted in the large pores without being lost during the coring process, indicating that the connectivity of pores and throats was poorer than type I. The pores were dominated by organic matter pores, but the formation mechanism was different from that of type I. The SEM images showed that the pores were formed due to the organic shrinkage (Fig. 13(a6) and 13 (b6)) (Feng et al., 2021). In addition, beaded organic matter pores can be observed from the SEM (Fig. 13(b6)). Intraparticle dissolution pores can also be seen in type II pore structures (Fig. 13 (a7), (b7), and (b8)). Structural vitrinite can be observed in this type of pore structure, which implies that the kerogen is mainly type III which mainly generates gas (Fig. 13(b5), 13 (b6), and 13 (b9)). The curves before and after extraction at large pore sizes are separated indicating the oil and gas generated by kerogen have not been expelled (Fig. 13(a3) and 13 (b3)).

Type III pore structure (Fig. 14(a)—(n)): the hysteresis loops were characterized by H2 and H3, indicating the complicated pore and throats and their connection (Fig. 14(a), 14(b), 14(h), and 14 (i)). When the samples were processed by methylene dichloride, no obvious change was displayed in the pore size distribution

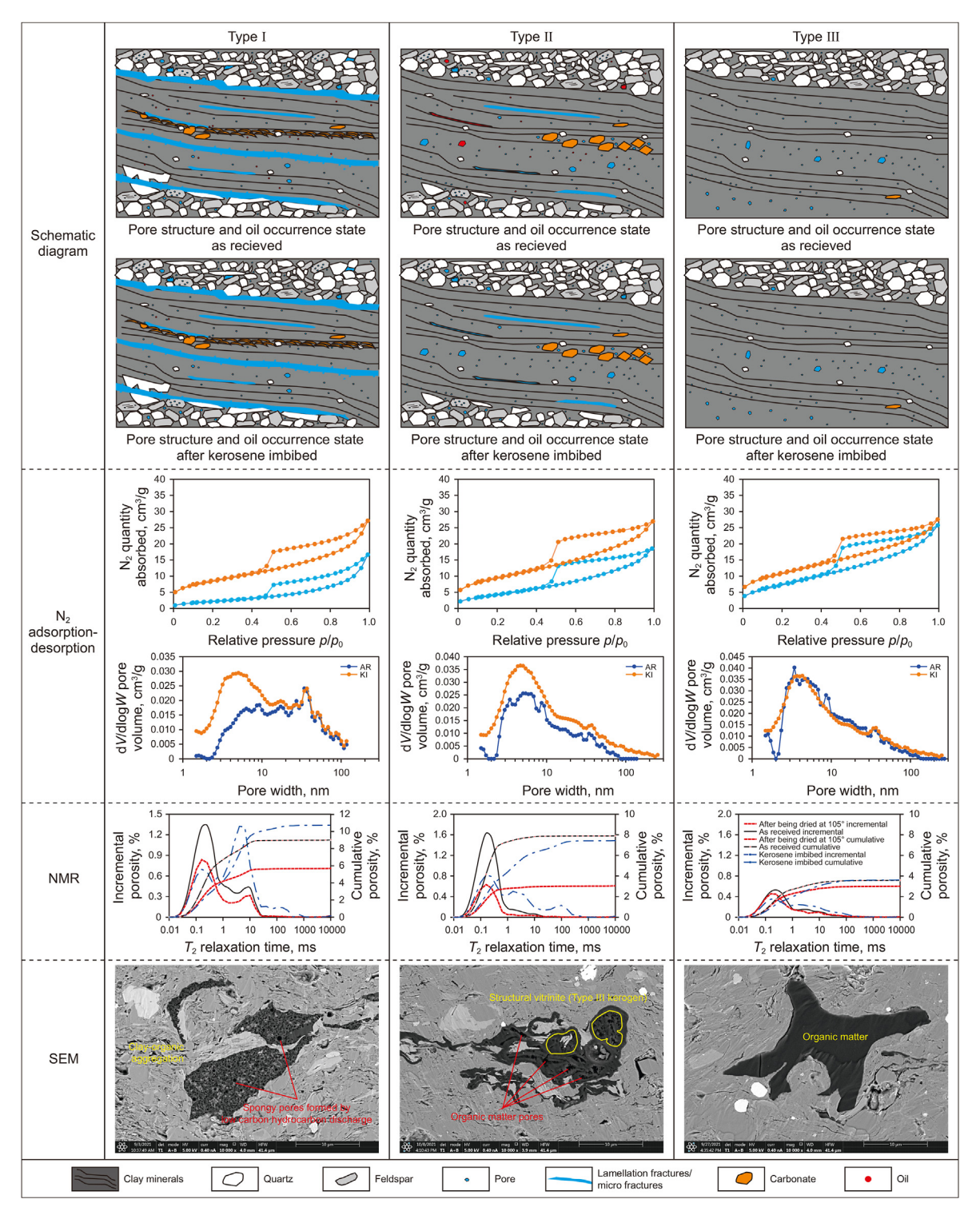


Fig. 16. Implications of pore structure types on shale oil.

(Fig. 14(c) and 14 (j)). Although the pores were still dominated by organic matter pores and intraparticle dissolution pores, the total volume of pores was the lowest in these three pore structure types (Fig. 14(c)–(g) and 14(j)–14(n)). There were barely any oil occurrences attributed to the poor pore structure. Additionally, the development of lamellation fractures can significantly improve the quality of pore structure (Figs. 12–14) (Wilson et al., 2015; Lai et al., 2022; Pang et al., 2022).

Fig. 15 shows most pores are distributed at short pore width (<10 nm), followed by 10-50 nm, and a few macropores (>50 nm). Compared with types II and III pore structures, type I pore structure is characterized by few micropores (<10 nm) and more mesomacro pores (>10 nm). Type II is better than type III according to the pore size distribution (Fig. 15(a)). After extraction with methylene dichloride, the pores shorter than 10 nm of type I increased, while type II and III were almost unchanged (Fig. 15(b)). Even

though the three types of pore structures showed different porethroat systems, the micropores (<10 nm) made the most contribution to the pore volume (Fig. 15).

4.3. Contribution of pore structures on hydrocarbon

Pore structure plays a crucial role in hydrocarbon generation, oil accumulation and immigration, and hydraulic fracturing (sources development) (Lai et al., 2018; Gou et al., 2019).

An abundance of large pore space (mainly lamellation fractures) is shown in type I pore structure, which is rich in oil. However, oil hosted in lamellation fracture is lost during coring process. Some oil enriched in the small pores, dominated by intraparticle dissolution pores, intercrystalline pores, organic matter pores, and organic-clay compound pores still retained. The change curves of N₂ adsorptiondesorption before and after dichloromethane extraction can verify this (Fig. 16). The amplitude of larger T_2 components rising after kerosene-saturated elucidates the same point (Fig. 16). More isolated pores are connected through lamellation fractures, which increase immigration pathways, enhance fracability, and improve engineering quality. In type II pore structure, lamellation fractures are relatively rare, mainly consisting of organic matter pores and clay mineral intercrystalline pores. Oil is enriched in these pores, but can not be expelled due to the high capillary pressure and strong mineral adsorption. Therefore, the pore volume corresponding to pore size distribution increased after dichloromethane extraction (Fig. 16). The porosity of the third type is the smallest and the main pores are intracrystallite pores and organic pores (Fig. 16). After hydrocarbon generation, sources can only exist in these spaces. Still, they can not immigrate to reservoirs, attributed to strong compression, high capillary pressure, clay mineral adsorption, and rare lamellation fractures. The quality and oiliness of this type of rocks are poor.

From the SEM observation shown in Fig. 16, the maturity of organic matter in type I pore structure is higher than in type II. The spongy organic pores in regular circle geometry indicate that the organic type is mainly Type II. The structural vitrinite (Gelatinized cell walls and residual cell cavities) implies the Type III kerogen, which is primarily gas-generating and derived from terrestrial plant material. Hydrocarbon expulsion to adjacent reservoirs is hindered due to a lower degree of thermal evolution. In addition, some organic pores generated by shrinking of organic during the thermal process can be observed (Fig. 4). All these pores characteristics and experimental curves under different conditions indicate that the rocks are going through different maturity, which in turn implicate the reservoir space feature and pore structures.

5. Conclusions

In conclusion, this study has integrated conventional techniques of pore structure evaluation, including SEM, MICP, 2D NMR, N_2 adsorption, and CT scanning to shed light on the pore characterization and pore structure classification, providing valuable insights into the implications for hydrocarbon and oil accumulation.

The dominant pore types are organic matter pores, intragranular pores and lamellation fractures. Lamellation fractures development have been identified as a key contributor to the connection of isolated pores and throats. The illite characterized by layered structure is shown to influence the formation of lamellation. The occurrence state of oil is mainly absorbed. The results of all experiments are consistent, showing abundant micropores (pore size is limited to 20 nm) exist in the organic-rich lacustrine depositional environment. N₂ adsorption is favorable for its high resolution for the assessment of nano-scale pores.

Three distinct pore structure types have been identified

according to these tests and analyses. Type I is distinguished by its highest porosity, the lowest surface area, and optimal conditions for hydrocarbon generation and oil accumulation. This type features spongy and honeycomb-shaped pores, with low-carbon materials infiltrating the adjacent reservoirs. The kerogen is classified as Type II, indicating a rich organic content, and the thermal maturity is notably high. Type II is characterized by a moderate pore volume and surface area, with the pore throat radius peaking at the apex and exhibiting a unimodal behavior in the NMR spectra of the original state. The kerogen is of Type III, derived from terrestrial plant material, and structural vitrinite is observed. Hydrocarbon expulsion to adjacent reservoirs is hindered due to a lower degree of thermal evolution. Type III, on the other hand, presents an independent pore structure with the least potential for hydrocarbon and oil enrichment. The pores are almost entirely isolated from each other, which impedes the migration and accumulation of hydrocarbons.

CRediT authorship contribution statement

Xiao-Jiao Pang: Writing — original draft, Methodology, Funding acquisition, Conceptualization. **Gui-Wen Wang:** Writing — review & editing, Supervision. **Yong-Jia Zhang:** Methodology, Data curation. **Da-Li Yue:** Writing — review & editing, Supervision. **Hong-Bin Li:** Methodology, Investigation. **Li-Chun Kuang:** Writing — review & editing, Supervision. **Chao-Liu Li:** Validation, Supervision.

Acknowledgments

This work is financially supported by the National Natural Science Foundation of China (Grant No. 42002133), Science Foundation of China University of Petroleum, Beijing (No. 2462024XKBH009, and the 2022 AAPG Foundation Grants-in-Aid Program, and China National Postdoctoral Science Foundation (BX20240425 and 2024M753611). The authors would like to express their sincere thanks to the PetroChina Daqing Company and PetroChina Research Institute of Petroleum Exploration and Development for their assistance in providing the data, and for their technical input to this work. My joint doctoral studies were funded by China Scholarship Council for one year. I am profoundly indebted to this. We are also grateful to reviewers for providing excellent advice on the manuscript.

References

- Anovitz, L.M., Cole, D.R., 2015. Characterization and analysis of porosity and pore structures. Rev. Mineral. Geochem. 80 (1), 61–164. https://doi.org/10.2138/ rmg.2015.80.04.
- Bai, L.H., Liu, B., Du, Y.J., et al., 2022. Distribution characteristics and oil mobility thresholds in lacustrine shale reservoir: insights from N₂ adsorption experiments on samples prior to and following hydrocarbon extraction. Petrol. Sci. 19 (2), 486–497. https://doi.org/10.1016/j.petsci.2021.10.018.
- Chalmers, G.R., Bustin, R.M., Power, I.M., et al., 2012. Characterization of gas shale pore systems by porosimetry, pycnometry, surface area, and field emission scanning electron microscopy/transmission electron microscopy image analyses: examples from the Barnett, Woodford, Haynesville, Marcellus, and Doig uni. Am. AAPG Bulletin 96, 1099—1119. https://doi.org/10.1306/10171111052.
- Chandra, D., Vishal, V., 2021. A critical review on pore to continuum scale imaging techniques for enhanced shale gas recovery. Earth Sci. Rev. 217, 103638. https:// doi.org/10.1016/j.earscirev.2021.103638.
- Chen, Y.F., Jiang, C.B., Leung, J.Y., et al., 2021. Multiscale characterization of shale pore-fracture system: geological controls on gas transport and pore size classification in shale reservoirs. J. Petrol. Sci. Eng. 202, 108442. https://doi.org/10.1016/j.petrol.2021.108442.
- Clarkson, C.R., Solano, N., Bustin, R.M., et al., 2013. Pore structure characterization of North American shale gas reservoirs using USANS/SANS, gas adsorption, and mercury intrusion. Fuel 103, 606–616. https://doi.org/10.1016/ j.fuel.2012.06.119.
- Feng, Z.H., Huo, Q.L., Zeng, H.S., et al., 2021. Organic matter compositions and organic pore evolution in Gulong shale of Songliao Basin. Pet. Geol. Oilfield Dev. Daqing 40 (5), 40–55. https://doi.org/10.19597/J.ISSN.1000-3754.202107012 (in

- Chinese).
- Gou, Q.Y., Xu, S., Hao, F., et al., 2019. Full-scale pores and micro-fractures characterization using FE-SEM, gas adsorption, nano-CT and micro-CT: a case study of the Silurian Longmaxi Formation shale in the Fuling area, Sichuan Basin, China. Fuel 253, 167–179. https://doi.org/10.1016/j.fuel.2019.04.116.
- Gou, Q.Y., Xu, S., Hao, F., et al., 2021. The effect of tectonic deformation and preservation condition on the shale pore structure using adsorption-based textural quantification and 3D image observation. Energy 219, 119579. https://doi.org/10.1016/j.energy.2020.119579.
- Gou, Q.Y., Xu, S., Hao, F., et al., 2023. Petrography and mineralogy control the nmµm-scale pore structure of saline lacustrine carbonate-rich shales from the Jianghan Basin, China. Mar. Petrol. Geol. 155, 106399. https://doi.org/10.2139/ ssrn.4448590.
- He, W.Y., Cui, B.W., Wang, F.L., et al., 2022. Study on reservoir spaces and oil states of the cretaceous Qingshankou Formation in Gulong sag, Songliao Basin. Geol. Rev. 68 (2), 693–741. https://doi.org/10.16509/j.georeview.2021.12.001 (in Chinese).
- He, W.Y., Liu, B., Zhang, J.Y., et al., 2023. Geological characteristics and key scientific and technological problems of Gulong shale oil in Songliao Basin. Earth Science 48 (1), 49–62. https://doi.org/10.3799/dqkx.2022.320 (in Chinese).
- Huangfu, Y.H., Zhang, J.Y., Zhang, S.C., et al., 2023. Characteristics of shale oil in different occurrence states of the Cretaceous Qingshankou Formation in the northern Songliao basin. Acta Geol. Sin. 97 (2), 523–538. https://doi.org/ 10.3969/j.issn.0001-5717.2023.02.015 (in Chinese).
- Ikeda, S., Nakano, T., Nakashima, Y., 2000. Three-dimensional study on the interconnection and shape of crystals in a graphic granite by X-ray CT and image analysis. Mineral. Mag. 64 (5), 945–959. https://doi.org/10.1180/ 002646100549760.
- Kamble, A.D., Mendhe, V.A., Chavan, P.D., et al., 2022. Insights of mineral catalytic effects of high ash coal on carbon conversion in fluidized bed Co-gasification through FTIR, XRD, XRF and FE-SEM. Renew. Energy 183, 729–751. https://doi.org/10.1016/j.renene.2021.11.022.
- Lai, J., Wang, G.W., Wang, Z.Y., et al., 2018. A review on pore structure characterization in tight sandstones. Earth Sci. Rev. 177, 436—457. https://doi.org/10.1016/ j.earscirev.2017.12.003.
- Lai, J., Liu, B.C., Li, H.B., et al., 2022. Bedding parallel fractures in fine-grained sedimentary rocks: recognition, formation mechanisms, and prediction using well log. Petrol. Sci. 19 (2), 554–569. https://doi.org/10.1016/j.petsci.2021.10.017.
- Li, J.J., Yin, J.X., Zhang, Y.N., et al., 2015. A comparison of experimental methods for describing shale pore features — a case study in the Bohai Bay Basin of eastern China. Int. J. Coal Geol. 152, 39–49. https://doi.org/10.1016/j.coal.2015.10.009.
- Li, J.Q., Lu, S.F., Zhang, P.F., et al., 2020. Quantitative characterization and microscopic occurrence mechanism of pore water in shale matrix. Acta Petrol. Sin. 14 (8), 979–990. https://doi.org/10.7623/syxb202008007 (in Chinese).
- Liu, B., Shi, J.X., Fu, X.F., et al., 2018. Petrological characteristics and shale oil enrichment of lacustrine fine-grained sedimentary system: a case study of organic-rich shale in first member of Cretaceous Qingshankou Formation in Gulong Sag, Songliao Basin, NE China. Petrol. Explor. Dev. 45 (5), 884–894. https://doi.org/10.1016/s1876-3804(18)30091-0.
- Liu, B., Wang, H.L., Fu, X.F., et al., 2019. Lithofacies and depositional setting of a highly prospective lacustrine shale oil succession from the Upper Cretaceous Qingshankou Formation in the Gulong sag, northern Songliao Basin, northeast China. AAPG (Am. Assoc. Pet. Geol.) Bull. 103 (2), 405–432. https://doi.org/ 10.1206/05021817416
- Liu, C., Xu, X.Y., Liu, K.Y., et al., 2020. Pore-scale oil distribution in shales of the Qingshankou Formation in the changling sag, Songliao Basin, NE China. Mar. Petrol. Geol. 120, 104553. https://doi.org/10.1016/j.marpetgeo.2020.104553.
- Liu, X.P., Lai, J., Fan, X.C., et al., 2020. Insights in the pore structure, fluid mobility and oiliness in oil shales of Paleogene Funing Formation in Subei Basin, China. Mar. Petrol. Geol. 114, 104228. https://doi.org/10.1016/j.marpetgeo.2020.104228.
- Liu, Z.S., Liu, D.M., Cai, Y.D., et al., 2020. Application of nuclear magnetic resonance (NMR) in coalbed methane and shale reservoirs: a review. Int. J. Coal Geol. 218, 103261. https://doi.org/10.1016/j.coal.2019.103261.
- Liu, Q., Sun, M.D., Sun, X.D., et al., 2023. Pore network characterization of shale reservoirs through state-of-the-art X-ray computed tomography: a review. Gas Science and Engineering 113, 204967. https://doi.org/10.1016/j.jgsce.2023.204967.
- Loucks, R.G., Reed, R.M., Ruppel, S.C., et al., 2012. Spectrum of pore types and networks in mudrocks and a descriptive classification for matrix-related

- mudrock pores. AAPG (Am. Assoc. Pet. Geol.) Bull. 96 (6), 1071–1098. https://doi.org/10.1306/08171111061.
- Mastalerz, M., Drobniak, A., Hower, J.C., 2021. Controls on reservoir properties in organic-matter-rich shales: insights from MICP analysis. J. Petrol. Sci. Eng. 196, 107775. https://doi.org/10.1016/j.petrol.2020.107775.
- Pang, X.J., Wang, G.W., Kuang, L.C., et al., 2022. Insights into the pore structure and oil mobility in fine-grained sedimentary rocks: the Lucaogou Formation in Jimusar Sag, Junggar Basin, China. Mar. Petrol. Geol. 137, 105492. https://doi.org/ 10.1016/j.marpetgeo.2021.105492.
- Pang, X.J., Wang, G.W., Nigel, M., et al., 2023. Prediction of lamina structure and reservoir quality in shale using well logs: The Cretaceous Qingshankou Formation, Gulong Sag, Songliao Basin, China. Geoenergy Science and Engineering 227, 211827. https://doi.org/10.1016/j.geoen.2023.211827.
- Shen, R., Qin, J.H., Xiong, W., et al., 2022. Study on pore structure and fluid mobility of shale oil in Jimsar Lucaogou Formation. J. Cent. S. Univ. 53 (9), 3368–3386. https://doi.org/10.11817/j.issn.1672-7207.2022.09.008 (in Chinese).
- Sigal, R.F., 2015. Pore-size distributions for organic-shale-reservoir rocks from nuclear magnetic-resonance spectra combined with adsorption measurements. SPE J. 20 (4), 824–830. https://doi.org/10.2118/174546-pa.
- Sing, K.S., Everett, D.H., Haul, R.A.W., et al., 1985. Reporting physisorption data for gas/solid systems with special reference to the determination of surface area and porosity. Pure Appl. Chem. 57 (4), 603–619. https://doi.org/10.1515/iupac.54.0530.
- Thommes, M., Kaneko, K., Neimark, A.V., et al., 2015. Physisorption of gases, with special reference to the evaluation of surface area and pore size distribution (IUPAC Technical Report). Pure Appl. Chem. 87 (9–10), 1051–1069. https://doi.org/10.1515/ci-2016-0119.
- Tiwari, P., Deo, M., Lin, C.L., et al., 2013. Characterization of oil shale pore structure before and after pyrolysis by using X-ray micro CT. Fuel 107, 547–554. https://doi.org/10.1016/i.fuel.2013.01.006.
- Vishal, V., Chandra, D., Bahadur, J., et al., 2019. Interpreting pore dimensions in gas shales using a combination of SEM imaging, small-angle neutron scattering, and low-pressure gas adsorption. Energy Fuel. 33, 4835—4848. https://doi.org/10.1021/acs.energyfuels.9b00442.
- Wang, Z.Y., Cheng, Y.P., Wang, G., et al., 2022. Comparative analysis of pore structure parameters of coal by using low pressure argon and nitrogen adsorption. Fuel 309, 122120. https://doi.org/10.1016/j.fuel.2021.122120.
- Washburn, K.E., Anderssen, E., Vogt, S.J., et al., 2015. Simultaneous Gaussian and exponential inversion for improved analysis of shales by NMR relaxometry. J. Magn. Reson. 250, 7–16. https://doi.org/10.1016/j.jmr.2014.10.015.
- Wilson, T.H., Smith, V., Brown, A., 2015. Developing a model discrete fracture network, drilling, and enhanced oil recovery strategy in an unconventional naturally fractured reservoir using integrated field, image log, and threedimensional seismic data. AAPG (Am. Assoc. Pet. Geol.) Bull. 99 (4), 735–762. https://doi.org/10.1306/10031414015.
- Wu, S., Yang, Z., Pan, S., et al., 2020. Three-dimensional imaging of fracture propagation in tight sandstones of the upper Triassic chang 7 member, ordos basin, northern China. Mar. Petrol. Geol. 120, 104501. https://doi.org/10.1016/j.marpetgeo.2020.104501.
- Xu, Y., Lun, Z.M., Pan, Z.J., et al., 2022. Occurrence space and state of shale oil: a review. J. Petrol. Sci. Eng. 211, 110183. https://doi.org/10.1016/ j.petrol.2022.110183.
- Yang, F., Ning, Z., Wang, Q., et al., 2016. Pore structure characteristics of lower Silurian shales in the southern Sichuan Basin, China: insights to pore development and gas storage mechanism. Int. J. Coal Geol. 156, 12–24. https:// doi.org/10.1016/j.coal.2015.12.015.
- Zhang, A.D., Wang, J.P., Wang, Y.C., et al., 2021. Reservoir space types and oil occurrence of Gulong shale in Songliao Basin. Pet. Geol. Oilfield Dev. Daqing 40 (5), 68–77. https://doi.org/10.19597/J.ISSN.1000-3754.202107034 (in Chinese).
- Zhao, P.Q., Wang, L., Xu, C.H., et al., 2020. Nuclear magnetic resonance surface relaxivity and its advanced application in calculating pore size distributions. Mar. Petrol. Geol. 111, 66–74. https://doi.org/10.1016/j.marpetgeo.2019.08.002.
- Zhao, T.X., Xu, S., Hao, F., et al., 2023. Differential adsorption of clay minerals: implications for organic matter enrichment. Earth Sci. Rev. 246, 104598. https://doi.org/10.1016/j.earscirev.2023.104598.
- Zhu, C.F., Guo, W., Li, Y.J., et al., 2021. Effect of occurrence states of fluid and pore structures on shale oil movability. Fuel 288, 119847. https://doi.org/10.1016/j.fuel.2020.119847.